UNIVERSITÀ
degli STUDI
di CATANIA

Dipartimento
di Fisica
e Astronomia
"Ettore Majorana"

MSc programme in physics

Clara Saia

Optimization of the light detection system of the ICARUS detector

---

final project

Supervisor:
Chiar.ma Prof.ssa Catia M. A. Petta

Co-Supervisor:
Dr. G.L. Raselli

---

academic year 2023/2024

Contents

Introduction

In the field of neutrino physics, some anomalies observed over the course of this century suggest the existence of a fourth type of neutrino: the sterile neutrino. As part of this research, the Short Baseline Neutrino (SBN) Program will study short-range neutrino oscillations at the Fermi National Accelerator Laboratory (FNAL) in Chicago.

This thesis work is carried out within the ICARUS experiment (Imaging Cosmic and Rare Underground Signals). The ICARUS detector is the world's largest liquid Argon Time Projection Chamber (LArTPC) and is the farthest and most sensitive detector in the SBN program for measuring muon and electron neutrino oscillations.

A key component of the ICARUS detector within the SBN Program is the Light Detection System. This system plays a key role in identifying the prompt scintillation light produced by neutrino interactions in the liquid Argon 600-tons active volume, providing precise timing information essential for the event reconstruction, the trigger system and the cosmic background rejection.

The Light Detection System is composed of 360 8-inch Hamamatsu R5912-MOD photomultiplier tubes (PMTs), installed within the two cryostats filled with liquid Argon. During a few years of operation at FNAL, under cryogenic conditions at temperatures around 87 K (-186 °C), the PMTs have suffered gain loss as an aging effect.

In a collaboration between the ICARUS researchers' teams of INFN Pavia and Catania, I implemented the experimental setup and performed the measurements of the PMT gain stability at room temperature and at

low temperature, using a climatic chamber at the INFN Catania Section. The measurements demonstrated that a single 8" Hamamatsu R5912-MOD PMT maintains a stable gain when operated at room temperature, while a consistent and permanent gain reduction was observed at -70 °C. Although this temperature is still significantly higher than that of liquid Argon, the results confirm a clear temperature dependent behavior in the PMT gain performance. In addition, strategies implemented in the ICARUS detector to address and reduce this effect are discussed.

The thesis is structured as follows.

- Chapter 1 provides a theoretical introduction to neutrino oscillations, including early experimental evidence and the anomalies that motivate the search for sterile neutrinos.
- Chapter 2 presents the Short Baseline Neutrino program and details the structure of the ICARUS T600 detector.
- Chapter 3 describes the ICARUS Light Detection System, including the scintillation properties of Argon, the design of the system, and the characteristics of the Hamamatsu R5912-MOD photomultiplier tube used.
- Chapter 4 analyzes the observed gain loss in the PMTs during cryogenic operation at FNAL and discusses the strategies implemented to mitigate these effects.
- Chapter 5 presents the experimental study carried out at INFN Catania, where PMT gain stability was tested using a climatic chamber. The results confirm stable gain at room temperature and significant degradation at low temperatures, offering insight into the long-term behavior of the system in cryogenic conditions. A simple model to explain and simulate the experimental observation is also presented.

Chapter 1

Neutrino Oscillations: a Brief Introduction

More than 90 years have passed since the famous Wolfgang Pauli letter, in which he hypothesized the existence of neutrinos as neutral particles in order to explain the continuous spectrum of beta decay as a three-body decay. Many of the neutrino properties and characteristics still need to be discovered. The neutrino itself, and in particular the study of its oscillations, is at the center of recent research projects in particle physics [1].

The neutrino is a particle with zero electric charge and very small mass. It has spin 1/2, half-integer as for all fermions, and it only exits with left-handed helicity. Furthermore, being a lepton, it does not interact strongly. Neglecting the gravitational interaction, it can only interact weakly through charged current (CC), exchanging $W^{\pm}$ bosons, and through neutral current (NC), exchanging Z^0 boson. The LEP measurement of the width of the invisible decay of the Z boson constrained to three the flavors of weakly interacting light neutrinos of the standard model [2, 3].

This chapter treats both the theoretical and the experimental aspects of neutrino oscillations. Furthermore, some experimental anomalies led to the implementation of a theory including the possible existence of a 4-th sterile neutrino are discussed.

1.1 Theoretical overview

The neutrino oscillation theory, first proposed in 1957 by Pontecorvo and later developed by Maki, Nakagawa, and Sakata in 1962, encountered over the years several experimental evidences [4].

In analogy to the Cabibbo-Kobayashi-Maskawa matrix, which describes the flavor change in quarks, it is possible to build up a neutrino mixing theory considering the three flavor eigenstates $|\nu_e\rangle$, $|\nu_\mu\rangle$ and $|\nu_\tau\rangle$ as a linear combination of the three mass' ones $|\nu_1\rangle$, $|\nu_2\rangle$ and $|\nu_3\rangle$:

$$|\nu_\alpha\rangle = \sum_{i=1}^{3} U^*_{\alpha i} |\nu_i\rangle \qquad\qquad \alpha = \{e, \mu, \tau\} \tag{1.1}$$

As well as:

$$|\nu_i\rangle = \sum_{\alpha=\{e,\mu,\tau\}} U_{\alpha i} |\nu_\alpha\rangle \qquad\qquad i = \{1, 2, 3\} \tag{1.2}$$

The unitary matrix $U_{\alpha i}$ elements represent the so called the Pontecorvo-Maki-Nakagawa-Sakata (PMNS) matrix.The typical parametrization of PMNS matrix is written in terms of matrices $R(\theta_{ij}, \delta_{ij})$, rotation in the i-j plane by an angle θ_{ij} and a possible phase δ_{ij}:

$$U = R(\theta_{23}) \cdot R(\theta_{13}, \delta_{13}) \cdot R(\theta_{12}) \tag{1.3}$$

θ_{12}, θ_{23}, and θ_{13} are the three real mixing angles; δ_{13} is the Dirac Charge Parity (CP) violating phase. CP violation in neutrino oscillations has not yet been observed experimentally. Majorana CP-violating phases α_1 and α_2 can be included to describe possible $\nu - \bar{\nu}$ oscillations:

$$U = R(\theta_{23}) \cdot R(\theta_{13}, \delta_{13}) \cdot R(\theta_{12}) \cdot diag(e^{i\alpha_1/2}, e^{i\alpha_1/2}, 1) \tag{1.4}$$

These phases are physically meaningful only if neutrinos are Majorana particles — i.e. if the neutrino is identical to its antineutrino — and do not enter into oscillation phenomena regardless. If experiments show this 3×3 matrix to be not unitary, a sterile neutrino or some other new physics models have to be required [2, 5, 4].

Neutrino Oscillation The time evolution of a mass eigenstate $|\nu_i(t)\rangle$ in a vacuum after a time t can be described by the relation:

$$|\nu_i(t)\rangle = e^{-iE_i t} |\nu_i(0)\rangle \qquad\qquad i = \{1,2,3\} \tag{1.5}$$

where E_i is the energy of the i-th mass eigenstate. Considering that, using natural units ($c = 1$ e $\hbar = 1$):

$$E_i = \sqrt{\mathbf{p}^2 + m_i^2} \tag{1.6}$$

In ultra-relativistic regime ($|\mathbf{p}| >> m_i$) and $|\mathbf{p}| \sim E$ the Equation 1.6 becomes:

$$E_i = \sqrt{\mathbf{p}^2 + m_i^2} \simeq p + \frac{m_i^2}{2p} \simeq E + \frac{m_i^2}{2E} \tag{1.7}$$

Using Equations1.1, 1.2 and 1.5 the temporal evolution of an eigenstate of flavor $|\nu_\alpha\rangle$ can then be written:

$$|\nu_\alpha(t)\rangle = \sum_{i=1}^{3} U_{\alpha i}^* |\nu_i(t)\rangle = \sum_{i=1}^{3} U_{\alpha i}^* e^{-iE_i t} |\nu_i(0)\rangle = \sum_{\beta=e,\mu,\tau} \sum_{i=1}^{3} U_{\alpha i}^* e^{-iE_i t} U_{\beta i} |\nu_\beta(0)\rangle \tag{1.8}$$

According to this theory the probability that a $|\nu_\alpha\rangle$ flavour neutrino is detected as another flavour $|\nu_\beta\rangle$ at the time t is:

$$\begin{aligned} P_{\nu_\alpha \to \nu_\beta} = |\langle \nu_\beta | \nu_\alpha(t) \rangle|^2 &= \sum_{j=1}^{3} \sum_{i=1}^{3} U_{\alpha i}^* U_{\beta i} U_{\alpha j} U_{\beta j}^* e^{-i\left(\frac{\Delta m_{ij}^2}{2}\frac{L}{E}\right)} = \\ &= \delta_{\alpha\beta} - 4\sum_{i>j} Re\{U_{\alpha i}^* U_{\beta i} U_{\alpha j} U_{\beta j}^*\} sin^2\Big(\frac{\Delta m_{ij}^2}{2}\frac{L}{E}\Big) + \\ &\quad + 2\sum_{i>j} Im\{U_{\alpha i}^* U_{\beta i} U_{\alpha j} U_{\beta j}^*\} sin\Big(\frac{\Delta m_{ij}^2}{2}\frac{L}{E}\Big) \end{aligned} \tag{1.9}$$

The oscillation depends on:

- L/E ratio. L stands for length, i.e. the distance traveled by neutrinos in the laboratory frame (*baseline*): L=t with c=1. E is the neutrino energy.

- $\Delta m_{ij}^2 = m_i^2 - m_j^2$ i.e. the mass square difference in eV^2 between the $|\nu_i\rangle$and $|\nu_j\rangle$ mass eigenstates.

Equation 1.9 is made up of three distinct terms. The first term represents the scenario in which no oscillations occur. The second term describes three-flavor oscillations with an amplitude given by

$$\text{Re}\left(U_{\alpha i}^* U_{\beta i} U_{\alpha j} U_{\beta j}^*\right)$$

multiplied by a phase factor

$$\frac{\Delta m_{ij}^2 L}{2E}.$$

The third term encapsulates the effect of CP violation; the CP-violating phase δ_{13} can be determined by comparing the oscillation probabilities of neutrinos and antineutrinos, i.e.[6],

$$P(\nu_\alpha \to \nu_\beta) \quad \text{versus} \quad P(\bar{\nu}_\alpha \to \bar{\nu}_\beta).$$

Thus far, the discussion has assumed that neutrino oscillations occur in a vacuum, where all flavors interact identically. However, when neutrinos traverse matter, there are modifications in the oscillation probabilities (Mikheyev–Smirnov–Wolfenstein effect [7, 8]). This modification is particularly significant in long-baseline experiments, such as those involving solar neutrinos traveling from the Sun to Earth or atmospheric neutrinos passing through the Earth before detection.

Moreover, the existence of neutrino oscillations proves that neutrinos actually have mass, contradicting the original assumption that they were massless. Experiments such as Super-Kamiokande [9] and Sudbury Neutrino Observatory [10] have demonstrated that neutrinos change flavor, which can only occur if they have non-zero mass. Furthermore, neutrino masses can be measured independently of oscillations through experiments that analyze the beta decay endpoint, such as the Karlsruhe Tritium Neutrino Experiment (KATRIN) [11].

1.1.1 Two-neutrino oscillation approximation

In the two-neutrino oscillation approximation, a useful simplification arises when the experiment is not sensitive to the influence of the third neutrino

flavor. Under this assumption, the oscillation dynamics can be effectively described by considering only two flavors (α and β). The matrix U can be rewritten as a rotation matrix with respect to an angle $\theta_{\alpha\beta}$, called *mixing angle*:

$$U = \begin{pmatrix} cos\theta_{\alpha\beta} & sin\theta_{\alpha\beta} \\ -sin\theta_{\alpha\beta} & cos\theta_{\alpha\beta} \end{pmatrix} \tag{1.10}$$

In this way, the expression of the probability depends on the mixing angle θ and the difference in mass squares Δm^2.

The probability of transition from one flavor state ν_α to another ν_β (with $\alpha \neq \beta$) is given by:

$$P_{\nu_\alpha \to \nu_\beta}(L, E) = \sin^2(2\theta_{\alpha\beta}) \sin^2\left(\frac{\Delta m^2}{4}\frac{L}{E}\right) \tag{1.11}$$

Similarly, the survival probability of a neutrino remaining in its original flavor state is:

$$P_{\nu_\alpha \to \nu_\alpha} = 1 - P_{\nu_\alpha \to \nu_\beta} \tag{1.12}$$

These probabilities illustrate the oscillatory nature of neutrino flavor transitions as a function of the ratio L/E, remembering that L is the *baseline*, i.e. the distance traveled by the neutrino, and E is its energy. The sinusoidal dependence highlights the periodic exchange of probability between flavor states.

A typical representation of this phenomenon is the plot of $P_{\nu_\alpha \to \nu_\beta}$ as a function of L/E for different values of Δm^2. This visualization provides insight into the experimental signatures of neutrino oscillations and helps to determine the fundamental parameters of the mixing process.

1.2 Experimental Evidences

The existence of neutrino oscillations has been confirmed by various experiments. The main ones are briefly described below.

Solar Neutrinos: Electron neutrinos are produced in fusion reactions that convert hydrogen into helium (via the pp chain) inside the Sun. In the 1960s, the pioneering Homestake experiment led by the Nobel Prize

Richard Davis revealed that the observed flux of electron neutrinos was only about a third of the predicted value, a discrepancy known as the solar neutrino problem. This issue was eventually resolved by the neutrino oscillation mechanism, which demonstrated that the missing electron neutrinos had transformed into other flavors. In 2001, the Sudbury Neutrino Observatory (SNO) in Canada confirmed this by measuring the total neutrino flux, including muon and tau neutrinos, from the Sun.

The analysis of solar neutrino data — obtained from experiments such as Homestake and especially the Sudbury Neutrino Observatory (SNO) — in combination with reactor experiments like KamLAND, has yielded the oscillation parameters $\theta_{12} \approx 34^\circ$ and

$$\Delta m^2_{21} = m^2_{\nu_2} - m^2_{\nu_1} \approx 7.4 \times 10^{-5}\,\text{eV}^2.$$

The parameter Δm^2_{21} is associated with solar neutrinos because these experiments are primarily sensitive to the oscillations driven by the mixing between the first two mass eigenstates. The long-baseline (large L/E ratio) of solar neutrinos ensures that the oscillation effects governed by Δm^2_{21} dominate, while contributions from the larger mass splitting (Δm^2_{31}) tend to average out [12, 10, 3].

Atmospheric Neutrinos: Atmospheric neutrinos are produced from the decay of cosmic-ray-induced pions in the atmosphere, following the chain:

$$\pi^+ \to \mu^+ + \nu_\mu \tag{1.13}$$

$$\mu^+ \to e^+ + \nu_e + \bar{\nu}_\mu \tag{1.14}$$

This process results in the production of both muon and electron neutrinos. The oscillations between these flavors have been observed in experiments such as Super-Kamiokande in Japan and MACRO at the Gran Sasso National Laboratories of the National Institute for Nuclear Physics (INFN) in Italy.

Measurements from these studies determined the oscillation parameters:

$$\theta_{23} \approx 45^\circ, \quad |\Delta m^2_{31}| = |m^2_{\nu_3} - m^2_{\nu_1}| \approx 2.5 \times 10^{-3}\,\text{eV}^2.$$

Both experiments provided strong evidence for neutrino oscillations, with a statistical significance of 5σ from MACRO and subsequently 6.2σ from Super-Kamiokande [13, 14].

All these experiments fall into the category of "long-baseline" studies, where the oscillation parameter satisfies:

$$\frac{L}{E} \leq 10^3\,\mathrm{m/MeV}, \quad \text{corresponding to} \quad \Delta m^2 \geq 10^{-3}\,\mathrm{eV}^2.$$

Additionally, neutrino oscillations have been observed in other settings, such as in the vicinity of **nuclear reactors** and **particle accelerators**.

1.2.1 Mass Hierarchy

The absolute masses of neutrinos, as well as the ordering of their mass eigenstates (the so-called mass hierarchy), remain unknown. While oscillation experiments have precisely measured the mass-squared differences, they provide information only about the relative differences between the mass states rather than their absolute values. Specifically, the parameter

$$\Delta m^2_{31} = m^2_{\nu_3} - m^2_{\nu_1}$$

is determined only in modulus,

$$|\Delta m^2_{31}| \approx 2.5 \times 10^{-3}\,\mathrm{eV}^2,$$

leaving uncertainty as to whether m_{ν_3} is greater or smaller than m_{ν_1}. This ambiguity defines two possible scenarios:

- **Normal Hierarchy (NH)**: $m_{\nu_1} < m_{\nu_2} < m_{\nu_3}$, where the third mass eigenstate is significantly heavier.
- **Inverted Hierarchy (IH)**: $m_{\nu_3} < m_{\nu_1} < m_{\nu_2}$, where the first two eigenstates are nearly degenerate and heavier than the third.

Current experiments, such as NOvA and T2K, provide hints favoring the normal hierarchy, but the question remains unresolved [15, 16, 17].

Future experiments, including DUNE and JUNO, aim to determine the hierarchy with high precision [18, 19].

Moreover, while neutrino oscillations probe mass differences, they do not reveal the absolute scale of neutrino masses. The best upper limit on the absolute neutrino mass comes from tritium beta decay experiments, such as KATRIN, which constrain

$$m_\nu < 0.8\,\text{eV} \quad \text{(at 90\% CL)}.$$

Cosmological observations, particularly from the cosmic microwave background and large-scale structure formation, place even tighter constraints on the sum of neutrino masses, with an upper limit of

$$\sum m_{\nu_i} \lesssim 0.12\,\text{eV} \quad \text{(Planck Collaboration, 2018)}.$$

These efforts aim to fully determine the neutrino mass spectrum in the coming years [20, 21].

1.3 Short-Baseline Neutrino Anomalies

Over the past decades, numerous experiments involving solar, reactor and accelerator neutrinos have provided strong evidence for the three-neutrino oscillation framework, with the latest results yielding the following parameters: $|\Delta m^2_{31}| = 2.5 \times 10^{-3}$ eV^2 and $\Delta m^2_{21} = 7.4 \times 10^{-5}$ eV^2 [3]. However, despite this remarkable success, several experimental results have challenged the standard oscillation paradigm, suggesting the possibility of new physics beyond the three known neutrino flavors.

A particularly intriguing set of discrepancies has been observed in short-baseline neutrino experiments, characterized by small values of the ratio $L/E \leq 1$ m/MeV. These anomalies include:

- **Reactor Antineutrino Anomaly:** Measurements of the flux of electron antineutrinos ($\bar{\nu}_e$) from nuclear reactors have consistently shown a deficit compared to theoretical predictions. The anomaly has been observed in multiple experiments, including Daya Bay, Double Chooz, and RENO.

- **LSND and MiniBooNE Anomalies:** The Liquid Scintillator Neutrino Detector (LSND) experiment at Los Alamos National Laboratory reported an excess of electron antineutrino events ($\bar{\nu}_e$) that appear in a muon antineutrino ($\bar{\nu}_\mu$) beam, suggesting possible $\bar{\nu}_\mu \to \bar{\nu}_e$ oscillations with a mass-squared difference of the order of $\Delta m^2 \sim 0.1 - 1$ eV^2. This result was later tested by the MiniBooNE experiment at Fermilab, which studied both neutrino and antineutrino oscillations at similar baselines. MiniBooNE also observed an excess of electron-like events in both modes, reinforcing the LSND anomaly but leaving open questions due to possible background contamination from photon-induced events.

- **Gallium Anomaly:** Gallium-based experiments designed to test solar neutrino detection - SAGE and GALLEX - used intense artificial neutrino sources to calibrate their response to electron neutrinos (ν_e). Suddenly, they observed a deficit of detected events compared to theoretical expectations.

The combination of these independent observations has led to significant interest in the possibility that a fourth neutrino state, a **sterile neutrino**, might exist. Unlike the three active neutrinos, which participate in weak interactions, a sterile neutrino would interact only via gravity and mix with the active neutrinos, modifying their oscillation probabilities. However, the interpretation of these anomalies is still debated, as some experiments designed to test them have not observed any significant deviations from the three-neutrino framework.

Moreover, global fits of short-baseline data have revealed tensions between the appearance ($\nu_\mu \to \nu_e$) and disappearance ($\nu_e \to \nu_e$, $\nu_\mu \to \nu_\mu$) experiments. Although experiments like LSND and MiniBooNE observe an excess of electron neutrinos, disappearance experiments such as MINOS+ and IceCube have not reported consistent deficits in muon neutrino fluxes, making it difficult to fit all results within a simple sterile neutrino model [3, 5, 22].

1.3.1 Search for Light Sterile Neutrinos

In the 3+1 neutrino scenario, the PMNS mixing matrix extends to:

$$\begin{pmatrix} |\nu_e\rangle \\ |\nu_\mu\rangle \\ |\nu_\tau\rangle \\ |\nu_s\rangle \end{pmatrix} = \begin{pmatrix} U_{e1} & U_{e2} & U_{e3} & U_{e4} \\ U_{\mu 1} & U_{\mu 2} & U_{\mu 3} & U_{\mu 4} \\ U_{\tau 1} & U_{\tau 2} & U_{\tau 3} & U_{\tau 4} \\ U_{s1} & U_{s2} & U_{s3} & U_{s4} \end{pmatrix} \begin{pmatrix} |\nu_1\rangle \\ |\nu_2\rangle \\ |\nu_3\rangle \\ |\nu_4\rangle \end{pmatrix} \tag{1.15}$$

The mixing matrix can be decomposed as:

$$U = R(\theta_{34}) \cdot R(\theta_{24}, \delta_{24}) \cdot R(\theta_{14}) \cdot R(\theta_{23}) \cdot R(\theta_{13}, \delta_{13}) \cdot R(\theta_{12}, \delta_{12}). \tag{1.16}$$

For $\Delta m^2_{41} \gg |\Delta m^2_{31}|, \Delta m^2_{21}$, short-baseline oscillations can be approximated by a two-flavor oscillation formula:

$$P_{\nu_\alpha \to \nu_\beta} = \delta_{\alpha\beta} - 4|U_{\alpha\beta}|^2(\delta_{\alpha\beta} - |U_{\alpha\beta}|^2) \sin^2\left(\frac{\Delta m^2_{41} L}{4E}\right). \tag{1.17}$$

The distinctive dependence $\sin^2\left(\frac{\Delta m^2 L}{4E}\right)$ on the probability of the oscillation provides a unique signature that can help differentiate sterile neutrino oscillations from other potential explanations of the observed anomalies [5].

Each oscillation channel $\nu_\alpha \to \nu_\beta$ is driven by a different effective mixing angle $\theta_{\alpha\beta}$, namely:

$$\nu_\mu \to \nu_e: \quad \sin^2 2\theta_{\mu e} \equiv 4|U_{\mu 4}|^2|U_{e4}|^2 \qquad \text{(LSND, MiniBooNE anomalies)}; \tag{1.18}$$

$$\nu_e \to \nu_e: \quad \sin^2 2\theta_{ee} \equiv 4|U_{e4}|^2(1 - |U_{e4}|^2) \qquad \text{(reactor, gallium anomalies)}; \tag{1.19}$$

$$\nu_\mu \to \nu_\mu: \quad \sin^2 2\theta_{\mu\mu} \equiv 4|U_{\mu 4}|^2(1 - |U_{\mu 4}|^2) \qquad \text{(no anomaly observed)}. \tag{1.20}$$

Notice that short-baseline transitions $\nu_\mu \to \nu_e$ require both U_{e4} and $U_{\mu 4}$ to be non-zero, necessarily implying that the survival probabilities of ν_μ and ν_e are less than one. This parameter dependence enables further constraints on the parameter space by simultaneously observing the appearance of ν_e along with the disappearance of ν_e and ν_μ at a short-baseline [5].

1.3.2 Experimental Status and Future Prospects

Several experiments are actively investigating short-baseline anomalies. Among these, the main focus will be the Short-Baseline Neutrino Program (SBN) at the Fermi National Accelerator Laboratory. The objective is to definitively test eV-scale sterile neutrinos by minimizing systematic uncertainties with identical liquid Argon detectors at different distances. Its ability to distinguish ν_e from photon backgrounds is crucial to resolving the MiniBooNE anomaly [22].

Looking ahead, future neutrino facilities such as DUNE (Deep Underground Neutrino Experiment) could provide complementary tests of the sterile neutrino hypothesis with long-baseline beams and improved detector technology. Furthermore, new reactor neutrino experiments with near and far detectors may further refine our understanding of the reactor anomaly [18].

In conclusion, ongoing and upcoming experiments offer a decisive opportunity to resolve long-standing short-baseline anomalies and determine whether sterile neutrinos play a fundamental role in neutrino oscillations.

Chapter 2

The Short-Baseline Neutrino Program and ICARUS T600

2.1 Short-Baseline Neutrino program

The Short-Baseline Neutrino (SBN) Program at the Fermi National Accelerator Laboratory (FNAL) was designed to study neutrino oscillations at short baseline and from that eventually evaluate the existence of a 4-th sterile neutrino at the eV-scale. [5]. It consists of 3 consecutive Liquid Argon Time Projection Chambers (LAr-TPCs): SBND, MicroBooNE and ICARUS. They are respectively 110 m, 470 m, and 600 m far from the target of the ν_μ (or $\bar{\nu}_\mu$) 8 GeV BNB. They are different in dimensions, ICARUS, the Far Detector, is the largest - and they subtend all the same solid angle. In table 2.1 the detector-target distances and the LAr masses

Detector	**Distance**	**Active LAr Mass**	**Total LAr Mass**
SBND	110 m	112 ton	220 ton
MicroBooNE	470 m	87 ton	170 ton
ICARUS	600 m	476 ton	760 ton

Table 2.1: *In the table, distances from the BNB target and active and total LAr masses of the detectors*

(total and active) are listed [22].

The SBN project is sensitive both to neutrino appearance and disappearance channels. Some examples of neutrino oscillation probability as a function of the baseline and the energy are shown in Fig. 2.1. It will also perform $\nu - Ar$ interaction cross section studies at the GeV energy scale but also sub-GeV Dark Matter searches and other BSM Physics, such as the violation of the Lorentz and CPT symmetry.

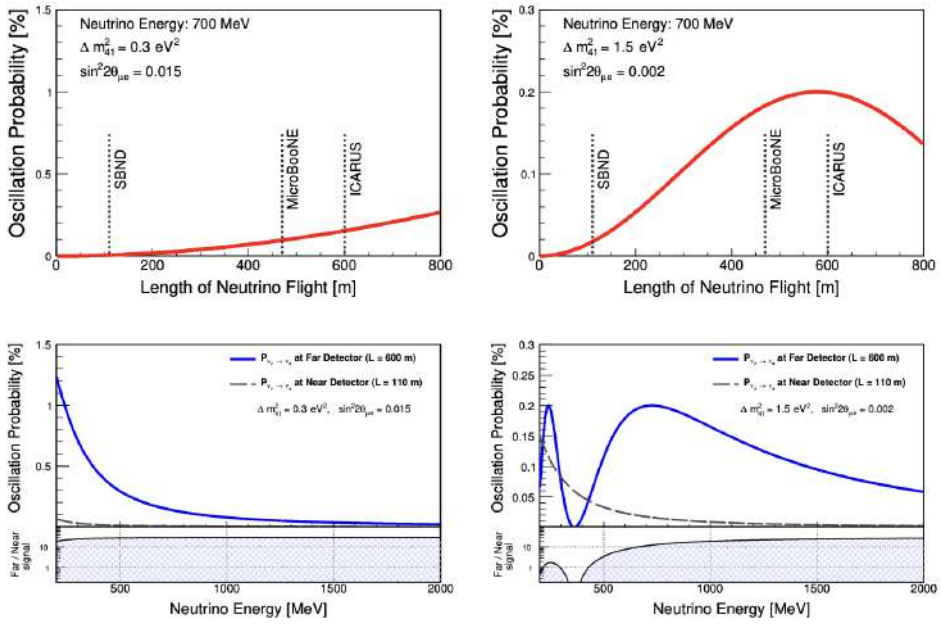

Figure 2.1: *The upper panels display the $\nu_\mu \rightarrow \nu_e$ oscillation probability for a 700 MeV neutrino as a function of the baseline, considering two different possible Δm^2_{41}. The lower panels illustrate the $\nu_\mu \rightarrow \nu_e$ oscillation probability at distances of 110 m and 600 m as a function of neutrino energy at the same Δm^2_{41} [5].*

In addition, it will verify the most recent observations claimed by the Neutrino-4 experiment [23]. Beyond physical goals, it is important to observe the excellent capability to handle and improve the LAr-TPCs technology, which can be considered as the leading technique in the field of

neutrino physics, that will be used in the upcoming DUNE/LBNF detector design. [5, 24].

2.1.1 Booster Neutrino Beam

The Booster Neutrino Beam (BNB) is produced by bombarding a beryllium target with 8 GeV protons from the Booster Accelerator. Proton reactions on target produce hadrons, mainly positive pions π^+ [22].

The BNB is a predominantly muon-type neutrino beam. The ν_μ flux originates from the in-flight decay of charged pions ($\pi^+ \rightarrow \mu^+ + \nu_\mu$ and $\pi^- \rightarrow \mu^- + \bar{\nu}_\mu$) and, to a lesser extent, from kaon decay for energies greater than 2 GeV. The percentage of neutrinos produced depends on the beam energy: in general, the beam is composed of around ν_μ (93.6%) and $\bar{\nu}_\mu$ (5.9%). Charged secondaries are focused by a single toroidal aluminum horn that can focus either positive or negative particles and de-focus the other by changing its polarity. Focused mesons are allowed to propagate down a 50 m long, 0.91 m radius air-filled tunnel where the majority will decay, producing electron neutrinos ($\mu^+ \rightarrow e^+ + \nu_e + \bar{\nu}_\mu$ and $\mu^- \rightarrow e^- + \bar{\nu}_e + \nu_\mu$). The muons are stopped by 50 m of absorbing material. However, there is still contamination of ν_e and $\bar{\nu}_e$ at a level of 0.5%, for energies below 1.5 GeV. Of these, 51% comes from muon decay, while the remaining part comes from the decay of K^+ and K^0.

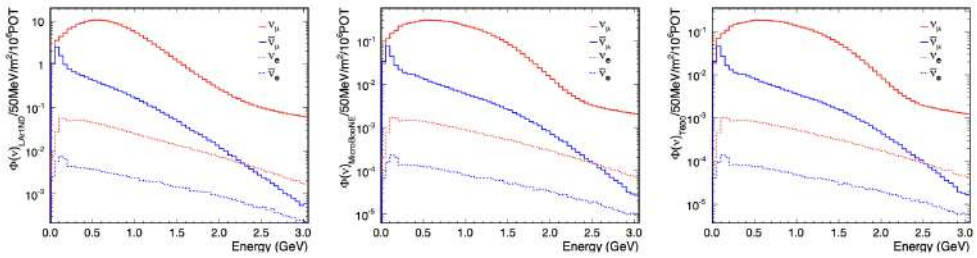

Figure 2.2: *From left to right, the BNB flux at SBND (LAr1-ND), MicroBooNE and (right) ICARUS-T600 depending on the energy [22]*

The neutrino spectrum is different at different distances. In Fig. 2.2 is shown the spectrum of fluxes ν and $\bar{\nu}$ that depend on neutrino energy for

the 3 detectors [22]. In Fig. 2.3 is shown the position of the SBN detectors aligned in the BNB direction.

2.1.2 Neutrinos at the Main Injector Beam

The T600 detector is also under the flux of Neutrinos at the Main Injector (NuMI) beam. The ICARUS detector is also exposed to NuMI at an angle of 6° off the axis, as shown in Fig. 2.3, providing a different neutrino energy spectrum that complements the data from the BNB. It will be used mainly to perform cross sections and interaction topologies $\nu_A r$ at energies relevant to the Long-Baseline Neutrino Facility (LBNF) program (0-3 GeV) [22].

The NuMI beamline is driven by 120 GeV protons from the *Main Injector* at Fermilab, delivering 4×10^{13} protons per pulse. This secondary beam is shaped by a double-horn focusing system, which enables various energy .

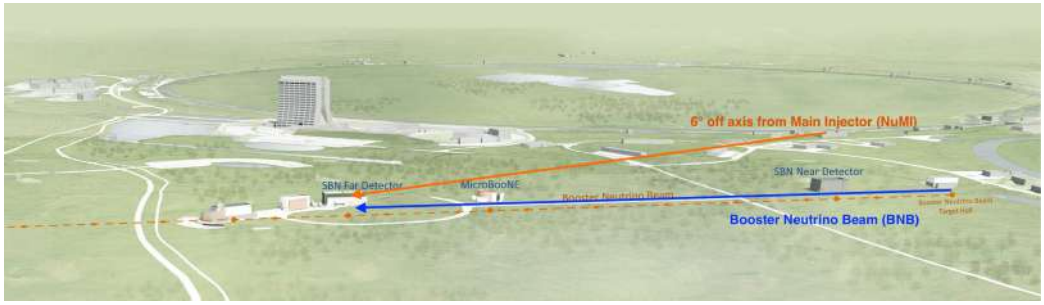

Figure 2.3: *Location of the SBN detectors and BNB and NuMi beam direction. [22].*

In table 2.2 BNB and NuMI collected POT during each ICARUS RUN from 2022 to 2025.

2.2 LAr-TPC technology

As already mentioned, the SBN detectors are all Liquid Argon Time Projection Chamber. This detection technique was proposed in 1977 by the

Collected Protons on target (Pot)	**BNB (FHC)** *positive focussing*	**NuMI (FHC)** *positive focussing*	**NuMI (RHC)** *negative focussing*
RUN1 (Jun 9 - Jul, 2022)	0.41×10^{20}	0.68×10^{20}	-
RUN2 (Dec 22 - Jul, 2023)	2.05×10^{20}	2.74×10^{20}	-
RUN3 (Mar - Jul, 2024)	1.36×10^{20}	-	2.82×10^{20}
RUN4 (Dec 10, 2024 - Jul 12, 2025)	1.69×10^{20} *	-	-
TOTAL	5.51×10^{20}	3.42×10^{20}	2.82×10^{20}

Table 2.2: *BNB and NuMI collected POT during each ICARUS RUN from 2022 to 2025. *RUN4 data up to March 23 are used for the purposes of this thesis.*

Nobel Prize Carlo Rubbia. It give the possibility to join the large sensitive mass of electron detectors with the high resolution of the old bubble chambers [25] .

When a charged particle (e.g. produced by a neutrino interaction) arrives in the detector, it ionizes the Argon: a couple of ion-electrons are produced. The liquid Argon allows the free electrons produced by ionization to move in the liquid over distances of the order of a few meters because of the following Argon main features.

- the density (1.4 g/cm^3) which guarantees higher interaction;
- the very high degree of purity, due to an advanced purification system;
- high electronic mobility.

Furthermore, Argon can be easily cooled with nitrogen. Inside the cryostat, the Argon is kept at a temperature of 98 K, using a liquid nitrogen cooling system [22, 25] .

Another property of liquid Argon is the ability to generate scintillation light. This argument will be discussed in detail in Chapter 3 [22].

2.3 ICARUS T600

ICARUS detector is the Far Detector of the SBN program at FNAL. The detector, originally located at the Gran Sasso National Laboratory (LNGS) in Italy, was exposed to the CNGS (CERN Neutrinos to Gran Sasso) beam. This long-baseline neutrino beam, produced by the CERN SPS accelerator, traveled over 700 km underground to reach the detector. The primary objective of ICARUS in this configuration was to study neutrino oscillations; particularly it is sensitive to the ν_e appearance and disappearance channels, but also to the ν_μ disappearance channel (Fig. 2.5). Operating between October 2010 and December 2012, ICARUS collected data on neutrino interactions and cosmic rays, significantly contributing to long-baseline neutrino oscillation research [26, 27, 28]. After completion of

Figure 2.4: *Picture of the Far Detector Building*

its data collection at Gran Sasso, ICARUS was transported to CERN for upgrades between 2015 and 2017. The main improvements included:

- Enhancement of the liquid Argon purification system.
- Reduction of the cathode thickness to a few millimeters.
- Installation of a new light collection system.
- Upgrade of the TPC readout electronics.

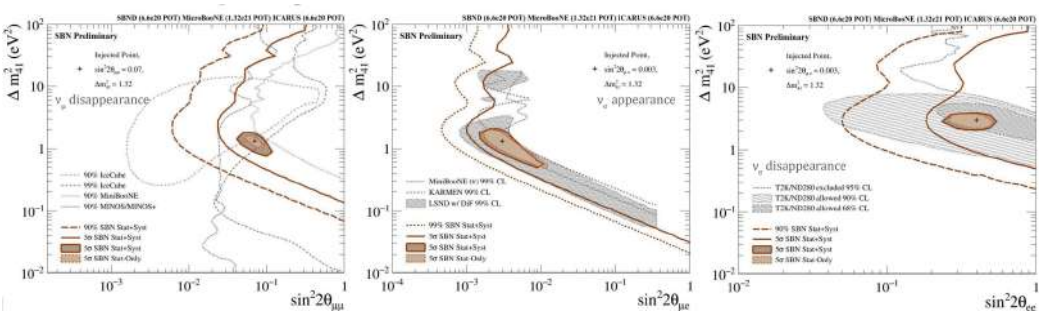

Figure 2.5: *The SBN exclusion and allowed-region sensitivities to ν_μ disappearance (left), ν_e appearance (center) and ν_e disappearance (right) under the (3+1) sterile neutrino hypothesis [29].*

Following these modifications, the detector was relocated to Fermilab in the United States, where it is now the Far Detector of the SBN program. Unlike its previous underground placement, ICARUS now operates at the surface, studying neutrinos from the BNB and NuMI off-axis beam. Being at the surface, the detector is now exposed to a much more significant cosmic ray flux. This increased presence of cosmic rays poses a challenge for the experiment, as they can mimic the signals produced by neutrinos [26, 27, 28].

2.3.1 TPC Structure

ICARUS-T600 is made up of two identical adjacent cryostats (T300 module), each containing two LAr-TPCs that share a common central cathode (Fig. 2.6). The external dimensions are $3.6 \times 3.9 \times 19.6\ m^3$ for each cryostat. In total, the detector is filled with 760 tons of ultra-pure LAr, of which only 480 tons are sensitive volume. In each module, electrons produced by ionizing particles in the Argon are drifted by a uniform electric field ($E_{drift} = 500\ V/cm$) towards the anodes, which consist of three parallel planes of wires. Those planes consist of a total of nearly 54000 9 m long threads, each oriented along one of three different directions: 0^o, $+60^o$, -60^o with respect to the horizontal. They are respectively called **Induction-1**, **Induction-2** and **Collection**. The charge induces signals on the first two in a non-destructive way, and is finally collected

Figure 2.6: *Picture (left) and scheme of one of the cryostat (right) [22, 30]*

by the last plane of wires. The electrons drift velocity in the TPCs is $v_{drift} = 1.6\ mm/\mu s$. In Fig. 2.7 is shown a scheme of the front view of the detector. From this scheme, it is easy to understand how the 3D geometrical reconstruction is performed on each TPC. Considering a track of an ionizing particle, we aim to detect the produced electrons. The point of impact on the three wire planes allows us to determine two spatial coordinates, while the third is obtained through the drift time. To achieve this, it is crucial to know with high precision the time t_0 at which an event occurs within the TPCs .

The ionizing particles in the LAr also produce scintillation light in the vacuum ultra-violet (VUV) range (λ = 128 nm), collected by the The Light Detection System that will play a key role in the reconstruction of time t_0. which will be discussed in chapter 3 [22, 31, 32].

2.3.2 The Cosmic Ray Tagger

As already mentioned, the main challenge for the ICARUS detector at shallow depth was the intense flux of the comics ray signal. To face up with this new experimental condition, a Cosmic Ray Tagger (CRT) system was added. It allows for "tagging", i.e. detecting spatially and temporally, the passage of incoming cosmic muons. This enables the detector to operate in anti-coincidence with the CRT signal, effectively discarding all cosmic muon tracks. Such an operation critically depends on knowing the arrival time of each muon with extreme precision [33].

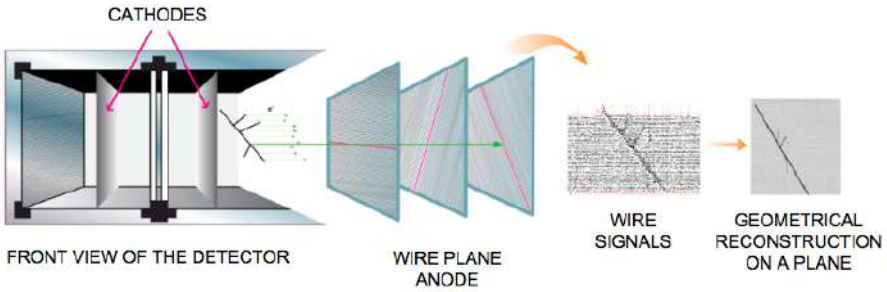

Figure 2.7: *Principle of operation of ICARUS-T600: the path of a charged particle in liquid Argon and its geometric reconstruction [22]*

The structure provides 99.9% coverage of the detector exterior. It is divided into three sections: top, bottom, and side, which respectively represent the upper, lower, and lateral coverage, each optimized based on the expected cosmic-ray rate from different directions. The three CRT sections consist of plastic scintillator modules coupled to silicon photomultipliers (SiPMs) or traditional photomultiplier tubes (PMTs) through appropriate WLS fibers [22, 33].

2.3.3 Installation of the Overburden

In June 2022, a 2.85 m thick concrete overburden was installed above the ICARUS detector to reduce the cosmic ray flux. This shielding plays a crucial role in improving the signal quality within the Time Projection Chamber (TPC), as it significantly decreases the number of recorded cosmic ray tracks, thereby reducing background noise and enhancing the ability to analyze neutrino interactions.

The impact of the overburden on cosmic ray attenuation can be observed in the average cosmic ray rate measured by the Cosmic Ray Tagger (CRT). Before installation, the nominal event rate of horizontally installed CRT modules was approximately 620 Hz, while vertically installed modules registered a rate of approximately 250 Hz. During the progressive construction of the concrete layers, continuous monitoring of the cosmic ray rate confirmed a gradual decrease. As shown in Fig. 2.8, after full installation of the overburden, the cosmic-ray rate in the top CRT mod-

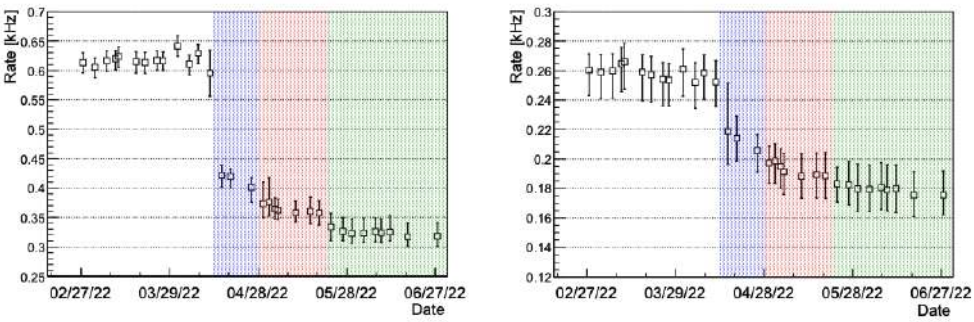

Figure 2.8: *Average CRT trigger rate as a function of time for a subset of Top horizontal CRT (left) and vertical CRT (right) the progressive installation of the 2.85 m of concrete overburden. Each colors correspond to the installation of* ~ 1 *m. Error bars represent the standard deviation over the modules. Taken from Refs. [33]*

ules dropped to around 330 Hz, whereas the vertical modules registered a reduced rate of about 180 Hz. This reduction is consistent with the expected removal of the soft electromagnetic component of cosmic rays by concrete shielding [33].

In addition to improving the TPC signal by filtering out a large fraction of cosmic rays, the reduction in cosmic ray flux is also essential for alleviating the stress on the Light Collection System, as it minimizes the number of unwanted light signals generated by cosmic interactions. With the completion of the overburden installation in mid-June 2022, the ICARUS detector started recording physics-quality data, benefiting from a cleaner event sample with a lower background contamination.

2.3.4 Some data about the Cosmic Ray Background

With current BNB intensities, one charged-current event is expected every 240 beam spills. The cosmic ray rate is significantly higher, on the order of 1 per 55 spills. Events that occur in coincidence with the acquisition time window are a source of disturbance. This time window coincides with the maximum drift time inside the TPC, which for the ICARUS detector is 0.96 ms. Another important factor to consider is the beam spill time

window of the BNB, which is only 1.6 μs [22].

The muonic background for ICARUS has been calculated through detailed simulations, obtaining a rate of $0.83 \cdot 10^6$ cosmic events per year (c/y) during the beam spill window and a total of approximately 11 cosmic ray tracks during the drift time window [33].

Chapter 3

ICARUS Light Detection System

3.1 Scintillation in Argon

When a charged particle interacts with the active LAr volume of a TPC, the Argon atoms can undergo to excitation and then emit a scintillation light through two main processes: *self-trapped exciton luminescence* and *recombination luminescence*. Both processes lead to the production of an excimer of Ar_2^*. This excimer decays, emitting vacuum ultraviolet (VUV) photons with a wavelength of approximately 128 nm. The emission process consists of two main temporal components:

- **Fast component**: associated with the decay of the *singlet state* of the excimer, with a lifetime of about 6 ns.
- **Slow component**: originating from the decay of the *triplet state*, with a lifetime of approximately 1.6 μs.

A scheme of the mechanism is shown in Fig. 3.1.

In particular,

- **Self-trapped exciton luminescence**: an incident charged particle directly excites an Argon atom (Ar^*), which then forms an Ar_2^* exited molecule combining with other Argon atoms.
- **Recombination luminescence**: ionization produces Argon ions (Ar^+) and free electrons. One Argon ion, combined with another Argon

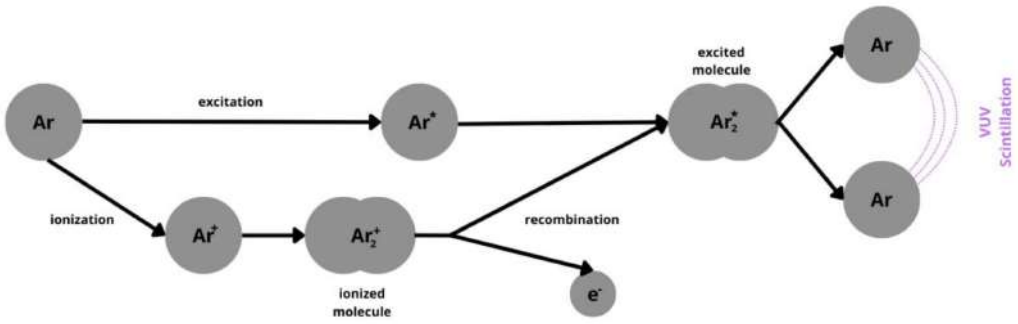

Figure 3.1: *Illustration of the scintillation process in liquid Argon, showing the formation and decay of excimers and the emission of UV light.*

atom, first produces an ionized molecule. An electron recombines with this ionized molecule, subsequently again generating Ar_2^*.

3.1.1 Argon Purity

Liquid Argon contains trace impurities that can affect various aspects of detector performance: some affect electron drift, others influence light transmission, and some impact both [34, 31]. In the ICARUS detector, a high level of purity is maintained through an advanced recirculation and purification system, which is crucial to ensuring optimal performance. For example, the concentration of electronegative molecules, such as oxygen and water, is kept below 0.1 parts per billion, allowing ionization electrons to drift over several meters without significant attenuation [22]. Additionally, the ultra-pure Argon used in the detector is highly transparent to its own scintillation light, preserving the efficiency of photon detection.

As a result of the liquid Argon production process, radioactive contaminants such as ^{39}Ar and ^{85}Kr are introduced. These isotopes decay primarily by β decay and, in general, can limit the sensitivity of LAr-TPC experiments aimed at detecting low-energy rare events, such as neutrinoless double beta decay or WIMP dark matter interactions [35]. However, in our detector, they do not represent a significant source of background.

Their presence is actually beneficial for testing the Light Collection System with signals consisting of only a few photoelectrons (see Section 4.1.1)

3.2 ICARUS Light Detection System

The transition from underground to shallow-depth operation for the ICARUS experiment required several significant modifications, primarily to address the challenge of the high cosmic-ray background [36, 31].

The ICARUS Light Detection System was completely upgraded by replacing the old 8″ ETL 9357FLA PMTs with new Hamamatsu R5912-MOD PMTs. The number of PMT passes from 74 ETL to 360 Hamamatsu, strongly increasing the granularity of the detection system. In addition, a new electronics system for the PMTs and a laser-based calibration system were introduced. This section will discuss the current state of the system, focusing on how these upgrades enable measurements at shallow depth [36, 31, 37, 38].

3.2.1 Structure and Goal

The Light Detection System is made up of 360 8″ PMT R5912-MOD. As it shown in the scheme in Fig. 3.2 and in Fig. 3.3 PMTs are located behind the planes of wires in T300 module, at the edges of the sensitive volume. In this way 90 PMTs are disposed on each wall [31, 32].

The system provides improved performance in terms of linearity, sensitivity (down to 100 MeV), time resolution (on the order of 1 ns), and increased granularity compared to the previous system used at LNGS [31]. The Light Detection System is used to:

- improve timing resolution of the events reconstruction: it allow to identify the occurrence time t_0 of each interaction inside the TPCs with O(ns) precision;

- improve spatial resolution of the events reconstruction: it is used to locate event along the longitudinal direction with O(m) precision.

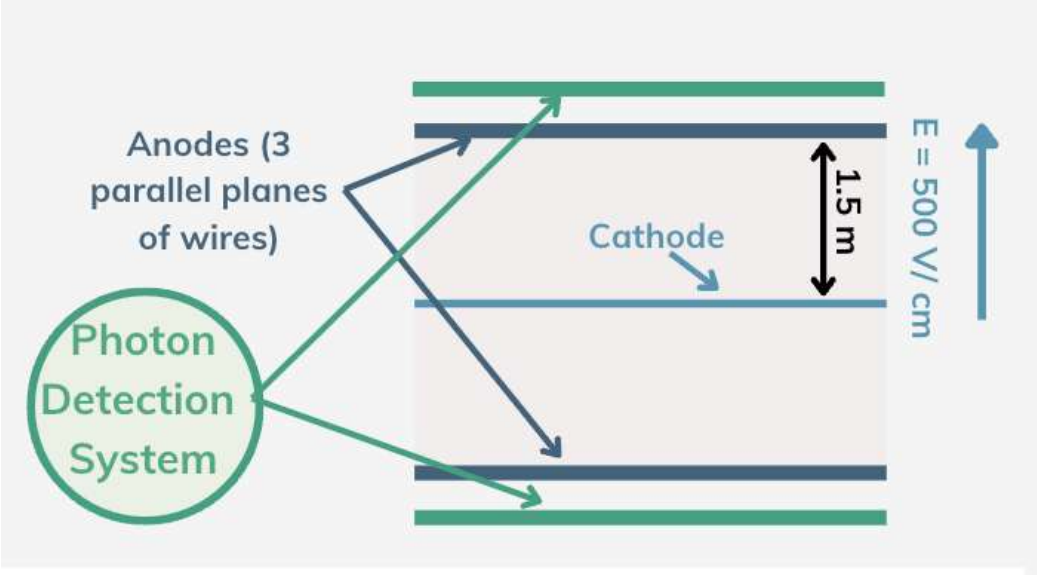

Figure 3.2: *Scheme of one T300 module underlying the positioning of the Light Detection System*

- It is a fundamental element for the trigger system, allowing in particular to detect signals from the huge cosmic ray background in order to perform a cosmic ray veto, in anti-coincidence with CRT signals.

Moreover, the Light Detection System could improve the in-time cosmic background rejection using the fine time structure of the beams. For instance, BNB does not emit continuously within the 1.6 μs spill window; instead, it consists of 84 pulses (bunches), with a bunch spacing of 19 ns (distance between the peak maxima), and a full width at half maximum of 2 ns. Of these 84 pulses, only 81 are active beam pulses, while 3 are empty. NuMI beam has a similar bunch structure. Since the resolution of the Light Detection System is of O(ns) precision (< 2 ns), after the upgrades carried out at CERN, the exact time t_0 at which an event occurs inside the TPCs is possible. Thus, by connecting the trigger system directly to the beam, cosmic-ray events occurring between peaks can be excluded, significantly reducing the overall number of background events [22].

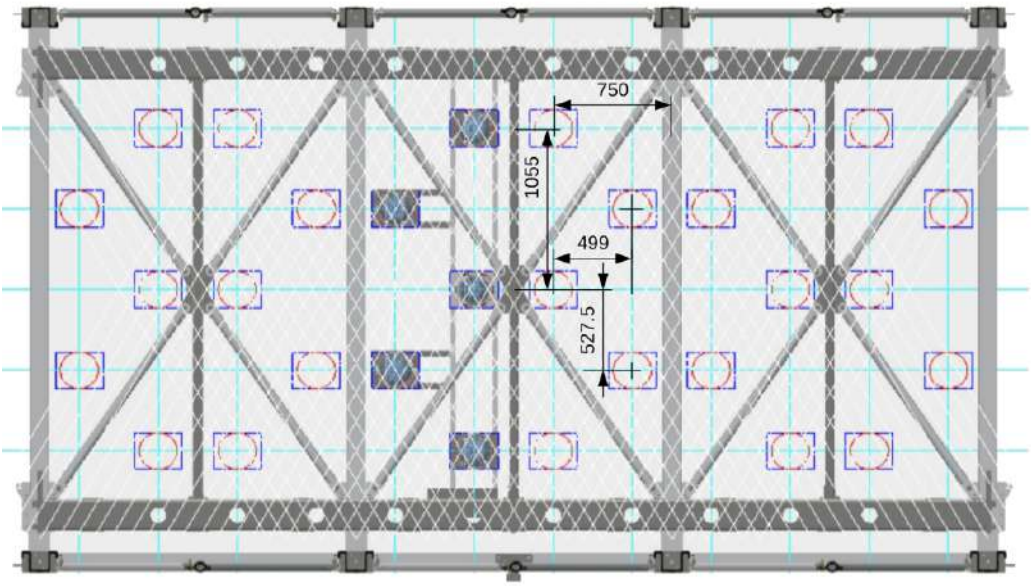

Figure 3.3: *Drawing of the PMT positioning behind a wire planes on the first 6 m of the mechanical frame [31].*

3.2.2 Light Detection System electronic set-up scheme

The electronic setup for ICARUS Light Detection System is designed to acquire and process signals from 360 Hamamatsu R5912-MOD PMTs. The system allows for continuous readout, digitization, and independent recording of the waveform signals from all PMTs. The core of the electronics consists of 24 CAEN V1730B digitizer boards. Each board is a 14-bit, 500 MSa/s [1] FLASH ADC with 16 channels and a 2 Vpp input dynamic range [39]. Each channel has 1024 consecutive buffers, capable of storing 5 kSa. Sampling at 500 MSa/s means recording one point every 2 ns, allowing an event to cover a time window of 5000 x 2 ns = 10 μs. When the board receives an external trigger signal (STOP), the active buffers are frozen, and the system shifts writing operations to the next available buffers. Data are read through the CONET2 protocol, which uses optical fibers to transfer information to a PC equipped with the CAEN A3818 board. In each board 15 channels are used for the acquisition of PMT

[1] MSa/s stands for Mega Sampling per second

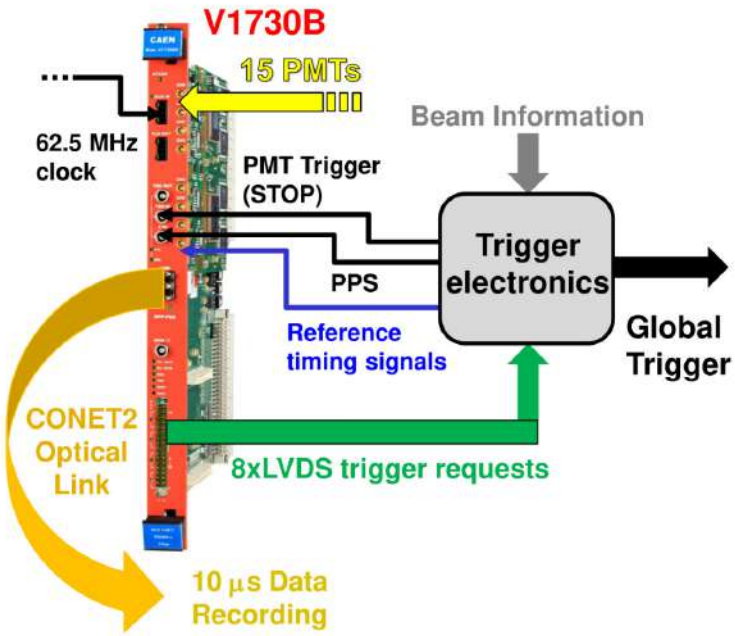

Figure 3.4: *Light Detection System system electronic set-up [40].*

signals (24 board x 15 channels cover 360 PMTs). The spare channel is left for the acquisition of ancillary signals, such as trigger pulses. The boards also generate a Low Voltage Differential Signal (LVDS) used in the detector trigger system.

3.2.3 PMT's Hamamatsu R5912-MOD

In this section, I will focus on the characteristics of the Hamamatsu R5912-MOD PMT, the object of the measurements of this thesis. However, before that, it is good to give a brief overview of the structure of this type of photosensors.

Photomultiplier Tube basic elements

A Photomultiplier Tube (PMT) operates by accelerating photoelectrons emitted from a photocathode to a series of dynodes, where each im-

pact generates secondary electron emissions. This cascade process significantly amplifies the initial signal, allowing even very weak photoelectric currents to be observed as a large output current at the anode.

The voltage divider in a PMT is responsible for establishing the appropriate voltage distribution across the dynodes. It typically consists of a resistive network that provides a graded voltage drop from the cathode to the anode. The design of the voltage divider can be adjusted to optimize the electron multiplication process. In some configurations, higher voltages are applied to the initial dynodes to enhance the primary multiplication stages, while lower voltages are used for the later stages to reduce noise and maintain signal stability. This non-uniform voltage distribution allows for improved performance in terms of gain stability and timing characteristics.

Gain

Considering a PMT with n dynode stages, when a voltage V is applied between the cathode and anode, the interstage voltage V_i applied to the i-th dynode depends on the PMT voltage divider scheme. It is possible to write the following expression, defining ϵ_i as the voltage divider ratio of the i-th dynode stage over the total V.

$$V_i = \epsilon_i V \qquad \textit{where} \quad \sum_{i=1}^{n} \epsilon_i = 1 \tag{3.1}$$

The secondary electron emission ratio δ_i for the i-th dynode is proportional to the interstage voltage applied V_i.

$$\delta_i = A_i V_i^{\alpha_i} \tag{3.2}$$

where A_i is and α are two constant term. In particular, α_i is a coefficient determined by the dynode material and geometric structure, ranging from 0.6 to 0.8. Usually, A and α are the same for each dynode:

$$\delta_i = A V_i^{\alpha} \tag{3.3}$$

The PMT *Gain* G is the total number of electrons collected at the anode per one photoelectron emitted by the photocathode. It can be define as:

$$G = \prod_{i=1}^{n} \delta_i = \prod_{i=1}^{n} A V_i^{\alpha} = \prod_{i=1}^{n} A(\epsilon_i V)^{\alpha} = V^{\alpha N} \prod_{i=1}^{n} A \epsilon_i^{\alpha} = K V^{\alpha N} \tag{3.4}$$

where $K = \prod_{i=1}^{n} A\epsilon_i^{\alpha}$ is a constant. For typical PMTs with 8 to 12 dynode stages, the anode output varies approximately with the 6th to 10th power of the applied voltage. A typical gain vs. voltage calibration curve for PMT Hamamatsu 5912 can be found in Fig. 3.5.

Dark Count Rate

Dark Count Rate refers to the rate of signals produced by the PMT in the absence of incident light. These signals are primarily caused by the spontaneous thermal emission of electrons from the photocathode or dynodes. At room temperature, metals can emit around 100 electrons per second per square meter, whereas semiconductors can reach up to 10^{10} electrons per second per square meter. When operating in current mode, the dark current affects the sensitivity of the device, especially in detecting very weak signals.

Quantum Efficiency

Quantum efficiency (QE) measures the probability that an incident photon on the photocathode will produce a photoelectron. In traditional PMTs, the quantum efficiency typically ranges from 20% to 30%, depending on the wavelength of incident light and the materials used in the photocathode.

Time Response

The time response of a PMT indicates how quickly the device can detect and amplify a short light pulse. Key parameters include the rise time, which is the time it takes for the anode current to transition from 10% to 90% of its peak value, and the transit time, which is the interval between the arrival of a light pulse in the photocathode and the corresponding current pulse in the anode. Typical transit-time values range from 40 to 60 nanoseconds, while the rise time is generally between 2 and 4 nanoseconds. The width of the peak in the transit-time distribution is the Time Transit Spread (TTS), usually ranging between 1-2 ns. A typical time response for PMT Hamamatsu 5912 can be found in Fig. 3.5.

Spectral Response

The spectral response describes the sensitivity of the PMT to different wavelengths of light. The composition depends on the photocathode and the entrance window of the device. For instance, some photocathodes are optimized to detect ultraviolet light, while others are more sensitive to visible or infrared light. A typical spectral response for PMT Hamamatsu 5912 can be found in Fig. 3.5.

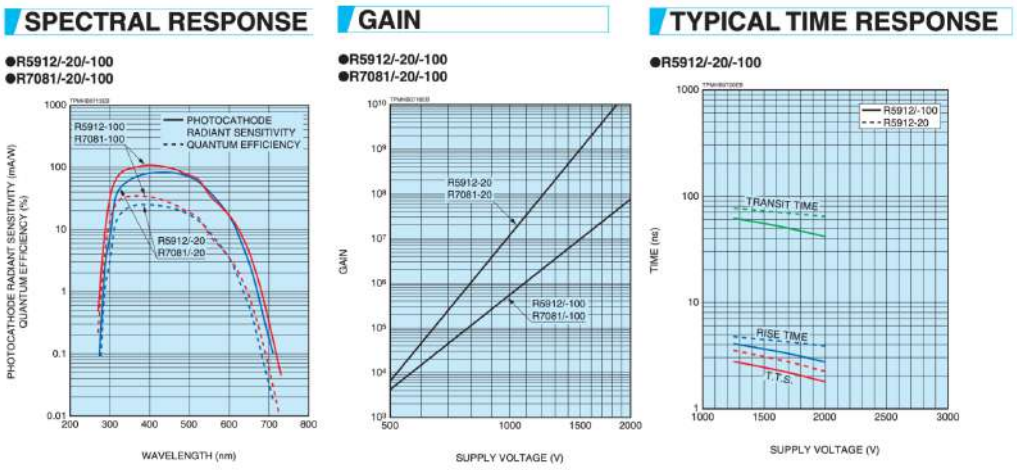

Figure 3.5: *Typical Spectral Response, Gain and time response for PMT R5912 [41]*

PMT's Hamamatsu R5912-MOD

The Hamamatsu R5912-MOD is a PMT of 10 dynode stages with an 8" hemispherical photocathode (see Fig. 3.6). It is derived from the parent model R5912 by depositing the bialkali photocathode on a platinum under-layer. This allows operation at temperatures as low as the liquid Argon temperature (87 K). This PMT model was selected after experimental tests on different detector samples from various manufacturers, such

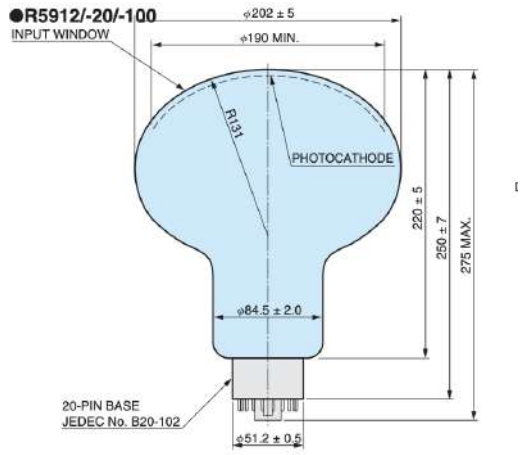

Figure 3.6: *Scheme of the PMT Hamamatsu R5912 taken from [41]*

as Hamamatsu and ETL. The nominal characteristics of the Hamamatsu R5912-MOD are summarized in Table 3.1.

Window	Hemispherical, 8 inches
Photocathode	Bialkali with Pt underlayer
Number of dynode stages	10
Typical gain	1×10^7 at 1500 V
Spectral response	300 ÷ 650 nm
Photocathode quantum efficiency (at 420 nm)	15 ÷ 16%
Maximum dark count rate*	$5000\, s^{-1}$
Nominal anode pulse rise time*	3.8 ns
Electron transit time*	54 ns
Transit time spread (FWHM)*	2.4 ns
Pulse gain saturation	Above 300 photoelectrons

Table 3.1: *Main characteristics of the Hamamatsu R5912-MOD. *Values for G = 1 × 10^7*

Hamamatsu delivered a preseries of 20 samples in 2015 for compliance testing, followed by 380 units in 2016. Before installation, PMTs were coated with 200 $\mu g/cm^2$ of Tetraphenyl Butadiene (TPB) as awavelength shifter, to convert vacuum ultraviolet (VUV) photons into visible

light. Each PMT was equipped with a dedicated base circuit designed according to the voltage distribution ratio recommended by Hamamatsu, providing high voltage to the grids, dynodes and anodes while allowing direct signal pickup from the anode. Although PMTs were selected to meet performance requirements at room temperature, all units have been immersed in liquid nitrogen at the factory to certify their mechanical strength at cryogenic temperatures. Afterwards, test measurements at cryogenic temperature were carried out at CERN, immersing a small sample of PMTs in liquid Argon to evaluate any parameter variation which could affect the scintillation light detection. In particular, gain as a function of the bias voltage was tested. The test results allowed us to choose the 360 best performing PMTs over the 400 tested, in order to use those for the detector.

Tests confirmed good linearity up to at least 100 photoelectrons (p.e.) and suitability for high illumination rates, as required by the ICARUS detector. Pulse gain saturation occurs above 300 p.e.. The electron transit time spread was approximately 1 ns, with minimal variation across the PMT window, both at room temperature and in cryogenic conditions [42, 43] .

These characteristics, along with the PMT's performance at cryogenic temperatures and resilience to magnetic fields, ensure that the Hamamatsu R5912-MOD meets the requirements of the ICARUS T600 Light Detection System [44, 41].

The PMT are biased by a negative High Voltage (HV), provided by CAEN A7030 boards. A laser system is used for temporal calibration and monitoring of each PMT channel, with fast laser pulses (60 ps FWHM, 405 nm) generated in the electronic alcove and distributed via optical fibers to each PMT [31].

Chapter 4

PMT Gain Loss and Mitigation Strategies

The ICARUS detector started the commissioning phase at FNAL in January 2021. The photomultiplier tubes (PMTs) were initially biased to achieve a nominal gain of approximately 0.7×10^7, at approximately 1500 V. Although the exact voltage varied slightly among individual PMTs, they were equalized to achieve a uniform mean gain. The calibration of the PMTs in the detector is repeated annually during the summer run stop. [40, 44, 45].

From the very beginning of detector operation, PMTs exhibited a significant gain reduction, which we will discuss in detail in this chapter. First, we will explain how the gain is determined.

4.1 Gain determination

4.1.1 Single Electron Response

When the photocathode converts a photon into a photoelectron (p.e.), it is then multiplied by the dynode chain. Recalling that the gain is the total number of electrons collected at the anode per one photoelectron emitted, it can be determined by measuring the so-called Single Electron

Response (SER). This represents the charge distribution corresponding to the amplification of a single photoelectron emitted by the photocathode.

The number of photons hitting a photocathode is a Poisson distributed variable with average μ. At the same time, the response of the multiplicative dynode system gives a Gaussian contribution. As a convolution of these contributions, the final response of a PMT, in an ideal noiseless condition, follows a charge distribution like [46]:

$$S_{ideal}(x) = \sum_{n=0}^{\infty} \frac{\mu^n e^{-\mu}}{n!} \frac{1}{\sigma\sqrt{2\pi}} \exp\left[-\frac{(x-nq)^2}{2n\sigma^2}\right] \tag{4.1}$$

in this expression, the sum runs over n, the effective number of p.e. emitted. For each n, we have a Gaussian contribution with mean nq and $\sigma_n = \sqrt{n} * \sigma$, that is, for the single photoelectron $n = 1$. The first Gaussian has mean q, which corresponds to $q = Gain/e$ (where e is the elementary charge 1.602×10^{-19}C).

This is the crucial point. In the graphs in Fig. 4.1, we can see experimental measurements of a PMT at a constant voltage but under different luminosity conditions. Since this is a real, non-ideal case, there is a pedestal given by electronic noise, which is present even in the absence of a light source. This signal can often be fitted with a Gaussian followed by an exponential tail. The first plot shows the Single Electron Response (SER) condition, with $\mu = 0.14$ $p.e.$. If we can achieve such a low illumination conditions to achieve at most only one photoelectron emitted, then we will observe only a Gaussian single-photoelectron peak convoluted with the background. Reasonably, under low illumination conditions, we obtain a situation similar to that in the second graph, on the right, where $\mu = 1.75$ $p.e.$. Under these conditions, we can see the contribution of up to 4 photoelectrons simultaneously converted by the photocathode and multiplied by the dynode chain (photopeaks). The first peak position allows the determination of the gain. However, with higher luminosity conditions, deconvolution of the Gaussian photopeaks becomes more difficult.

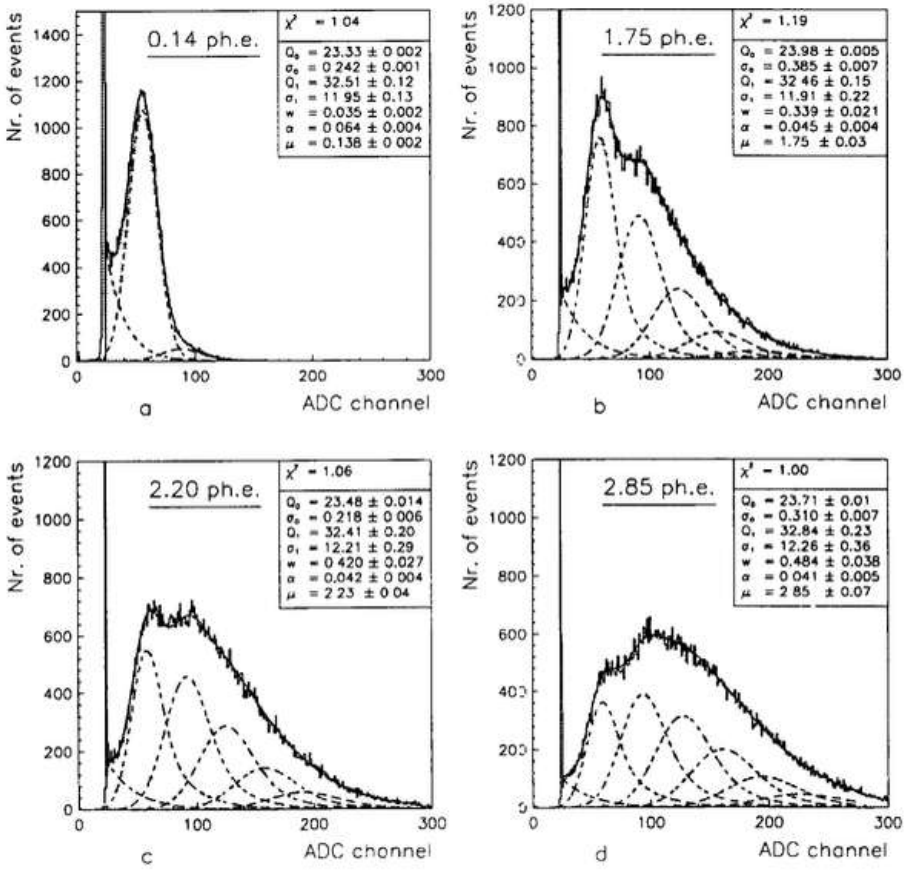

Figure 4.1: *Example of SER at a constant voltage and different LED intensities, as reported in literature [46]*

4.1.2 Gain measurement at FNAL

We can use the background photons from Argon to determine the gain of each PMT. We extract the Single Photoelectron Response (SPR) waveforms, which are the single-photon pulses digitized over time. The integral of these waveforms (appropriately calculated) allows us to obtain the SER. We could also perform the gain measurement using the laser system, even if the deconvolution is more complex due to a more intense light source; moreover, the laser energy calibration system needs further optimization.

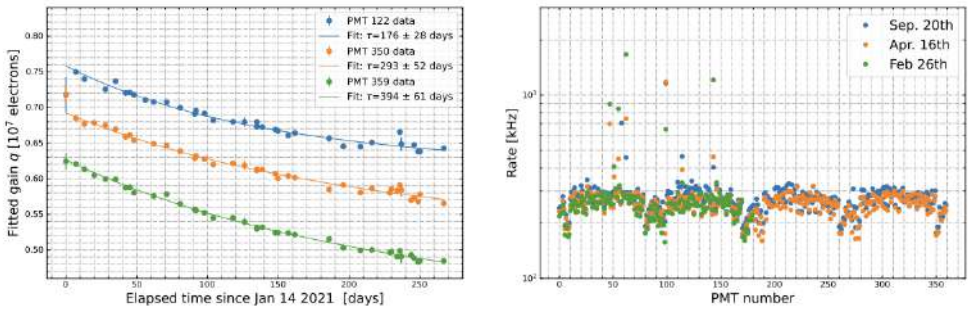

Figure 4.2: *Left: Preliminary measurements of PMT gain from January to November 2021 for 3 PMTs: ∼15% gain loss in 250 days. They are fitted through an exponential function* $f(x) = \frac{a}{1-exp[(x-b]/\tau]}$*, where a and b are constants and* τ *is the decay constant.*
Right: Rate of PMT optical pulses over 2 mV as a function of the PMT number for three different time moments: February, April, September 2021 [A. Scarpelli analysis]

4.2 PMT Gain Loss

As mentioned, the PMTs exhibited a gain loss when operating at the cryogenic temperature of 87 K in liquid Argon, as shown in Fig. 4.2 (left). Specifically, a gain loss of approximately 15% was observed over 250 days (1.93% per month), with an estimated output charge of approximately 7 C over 6000 hours of operation. The loss is not present at room temperature. Furthermore, if we measure the rate of background photons, optical pulses, over time, as shown in Fig. 4.2 (right), no similar variations are observed. This supports the idea that the loss is due to gain reduction and not to a decrease in the photocathode quantum efficiency, as the efficiency losses would have been visible in this second plot.

After turning off PMTs for 20 days, a slight gain recovery was observed, with an increase of 1-2% compared to the expected trend. This was originally interpreted as a fatigue effect, suggesting that the period of inactivity helped to partially restore the lost gain.

4.2.1 Initial Hypotheses and Testing Approaches

Subsequent testing at low temperature (-70 °) was performed at the Hamamatsu Q&A Labs and confirmed similar levels of gain reduction. It was noted that pre-installation tests did not include long-term performance studies under cryogenic conditions. The leading hypothesis for the observed gain degradation was related to the high charge accumulation affecting the dynode chain at low temperature. In particular, the secondary electron emission ratio δ of the dynode material, at cryogenic temperatures, when subjected to a high current, was suspected to degrade over time, leading to a progressive, cumulative, loss of gain.

To further investigate this phenomenon, additional stress tests were implemented in parallel at INFN Catania, using a dedicated setup designed to mimic the operational conditions at FNAL. These tests aimed to isolate potential degradation mechanisms by systematically varying temperature, illumination levels, and applied voltage while monitoring the PMT response.

4.3 Impact of Overburden Installation

During the initial phase of operations, the PMTs were exposed to a high cosmic ray rate because of the shallow depth of the experiment. However, after the construction of a 2.85 m thick concrete overburden in June 2022 (start of RUN1), the cosmic-ray rate was significantly reduced, as detailed in Section 2.3.3 (Fig. 4.3). This change was correlated with a noticeable reduction in the rate of PMT gain loss, suggesting a link between gain degradation and the amount of incident light on the PMTs.

4.4 Overall Gain Reduction and Mitigation Strategies

One key observation was that despite the gain loss, all PMTs remained equalized, meaning they lost gain at the same rate throughout the system. To compensate for this degradation, an increase in voltage should

Figure 4.3: *Picture of the concrete overburden*

have been applied to restore the original gain. However, rather than fully restoring the initial gain level, the decision was made to operate at a slightly lower gain, thereby reducing the stress on the system. Each PMT has a unique voltage-gain curve, so the applied voltage was adjusted individually .

The reduction in gain was limited to avoid the following drawbacks. First of all, a lower gain results in weaker signals, making it harder to distinguish single photoelectron (SPE) events from electronic noise. This can lead to a loss of trigger efficiency, as real events may fail to exceed the trigger threshold, potentially discarding low-luminosity events and causing data loss. Additionally, the transit time spread (TTS) increases, degrading the time resolution and impacting the accuracy of 3D reconstruction using PMTs and TPCs. The energy reconstruction also suffers as the deposited energy estimation based on collected photoelectrons becomes less reliable, necessitating frequent recalibrations. Furthermore, weaker and slower signals can hinder the selection of beam-in-time events, making it more challenging to distinguish in-time cosmics from neutrinos and

worsening background rejection when combined with CRT .

During RUN1 and RUN2, the gain was reduced from 0.7×10^7 to approximately $0.46 \times 10^7 \pm 2.1\%$, which led to a substantial reduction in the gain loss rate from 1.93% per month to 0.64% per month [32].

4.5 Implementation of New Signal Cables

Starting from RUN3, further improvements were made by replacing the old 37-m-long RG316/U PMT signal cables with higher-performance alternatives: 28-m-long WL-195N cables. I actively participated in the testing and installation phases of these cables at FNAL (Fig. 4.4).

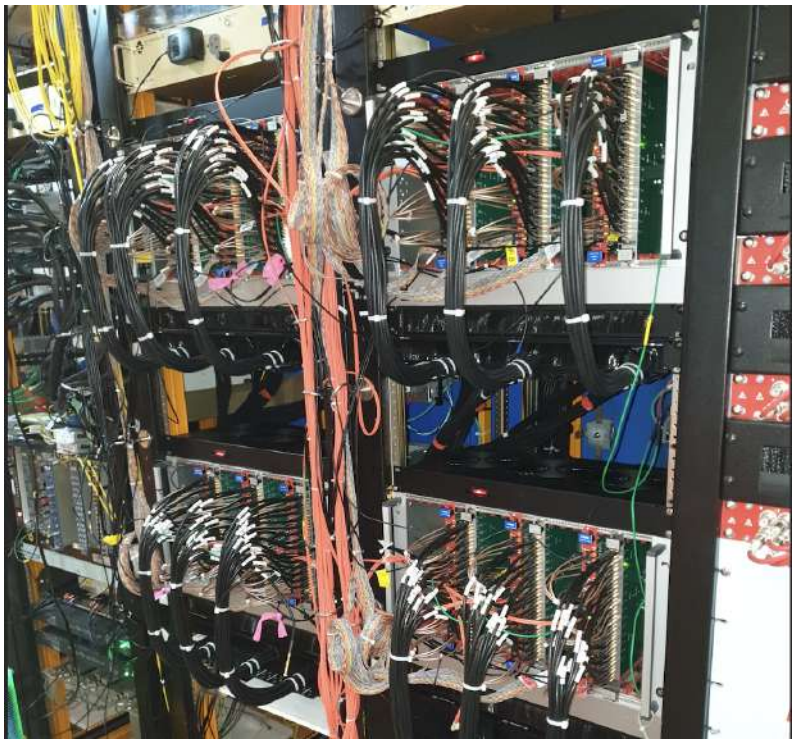

Figure 4.4: *A picture of CAEN V1730B digitizer boards with the new WL-195N cables.*

The effect of these new cables can be observed by comparing the PMT

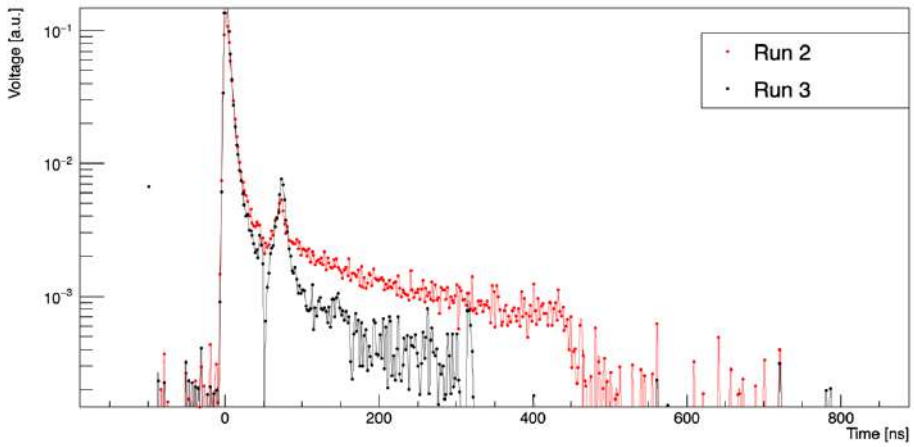

Figure 4.5: *SPR waveform for RUN2 and RUN3. Each Waveform is normalized respect to the integral.*

waveforms between RUN2 and RUN3, as shown in Fig. 4.5. In this plot, the amplitude of the SPR is shown as a function of time. As mentioned above, the SPR is connected to the gain. The plot exhibits a shorter tail in RUN3, as expected, due to the use of the new cables, which provide a faster time response. Furthermore, in RUN3, an average increase in signal amplitude was observed, indicating a higher amplitude and shorter duration, leading to an overall improvement in signal resolution .

This modification allowed for a further reduction in the applied voltage while maintaining efficient signal transmission. As a result, the average PMT gain was adjusted to $0.39 \times 10^7 \pm 1.5\%$, with a corresponding decrease in the gain loss rate to just 0.31% per month [32].

4.6 Summary of PMT Gain Loss

Table 4.1 provides an overview of the Light Detection System's performance across the years, highlighting the progressive average loss in PMTs gain.

	PMT Gain	Detector Modifications	PMT Gain Loss
Commissioning	0.7×10^7	Initial calibration	1.93% per month
RUN 1-2	0.46×10^7	Overburden installed Gain Reduction	0.64% per month
RUN 3-4	0.39×10^7	New signal cables 2-nd Gain Reduction	0.31% per month

Table 4.1: *Summary of PMTs gain variations over different operational runs.*

Chapter 5

PMT Gain Stability Measurements and Results

5.1 Introduction

To investigate the causes of the observed PMT gain loss, discussed in Chapter 4, in a collaboration between the ICARUS researchers' teams of INFN Pavia and Catania, I developed an experimental setup for PMT testing at both room and low temperatures. This chapter describes how the system was implemented, the performed measurements and the obtained results [32].

5.2 The Experimental Setup

To check the PMT gain stability at low temperature, we used the new CSN1-INFNCT environmental chamber. It has a high internal volume ($601 \times 810 \times 694 mm^3$) and is capable of reaching and controlling the temperature of -70 ° C. The selected PMT was a TPB-uncoated one, and we employed a continuous laser beam with a typical wavelength of 520 nm to illuminate it. Although the PMT has a peak sensitivity at 420 nm, its sensitivity at 520 nm remains sufficiently close to the peak value (see Section 3.2.3).

The measurement is performed in current mode, stressing the PMT with the maximum anodic current tolerated by its electronic base (approximately 28 μA). As shown in Fig. 5.1, the laser beam was transmitted through an optical fiber capable of operating at low temperatures. The laser was split into two optical fibers: one beam was attenuated using neutral density optical filters and then diffused over the PMT photocathode surface, while the other optical fiber was used for an independent reference measurement of the light via a bolometric photodetector. The temperature was measured using a Type-K thermocouple placed near the PMT photocathode.

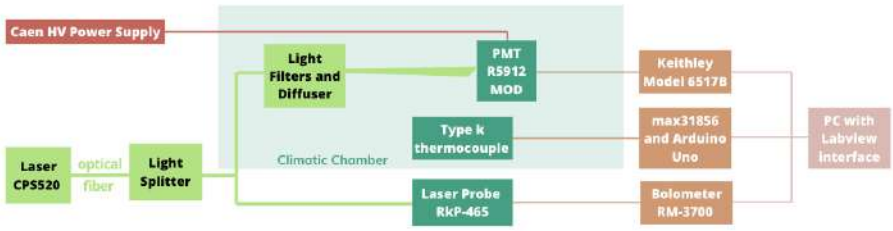

Figure 5.1:
Schematic of the experimental setup

The following instruments were used:

- Hamamatsu PMT R5912-MOD [41] powered by a CAEN N126 High Voltage Power Supply [47].
- Thorlabs Laser CPS520 [48] powered by a Philips PE1535 Bench Model Power Supply [49] at 5 V.
- Keithley 6517B digital multimeter [50].
- Laser Probe Inc. - Rm-3700 Universal Radiometer [51].
- Laser Probe Inc. - RkP-465 Silicon Power Probe [52].
- Analog Devices Inc./Maxim Integrated - MAX31856 Precision Thermocouple to Digital Converter and Type K Thermocouple [53].

- Angelantoni Test Technologies Sr - Climatic and Thermostatic Chamber DM340C.
- Mitsubishi Chemical Corp. - CK-120 optical fiber [54].
- Thorlabs Absorptive Neutral Density Filters.

5.2.1 PMT Characterization

A spare PMT, part of the original set of 400 PMTs tested but not selected for the final configuration of ICARUS, was used for this measurement. Figure 5.2 presents the measured relationship between gain and power supply voltage for this PMT unit. The gain determination was carried out during the 2018 testing phase at CERN, with a photon-counting equipment in order to acquire SPR charge spectra at room temperature, at different PMT HV (see Section 4.1.1).

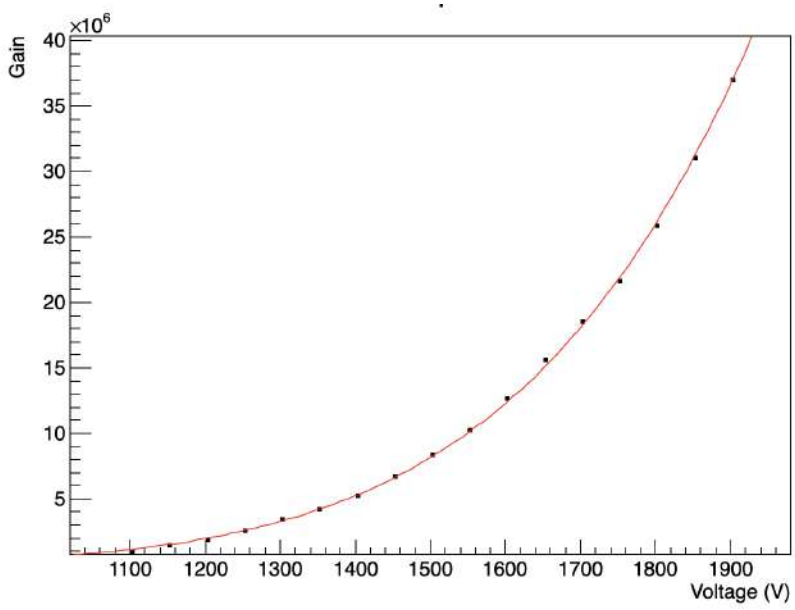

Figure 5.2: *Gain as a function of supplied voltage for the tested PMT. Data points are fitted with the typical behavior* $G = KV^{\alpha N}$*, with parameters:* $K = (4.8 \pm 0.2) \cdot 10^{-14}$ *and* $\alpha = 0.6358 \pm 0.0007$.

5.2.2 PMT Current Signal Reading

Figure 5.3 shows the PMT voltage divider scheme. The reference voltage distribution ratio is the standard suggested by Hamamatsu (Table 5.1) [41, 44]. To measure the current, resistor R27 was removed and the signal was extracted via a BNC cable. This signal was then sent to the Keithley 6517B digital multimeter, which directly acquired the current measurement. An oscilloscope was optionally used during the initial testing phase for waveform visualization. The multimeter was connected to the Data Acquisition (DAQ) Monitor via an RS-232 serial cable. The DAQ system was implemented using a LabVIEW interface (see Section 5.3).

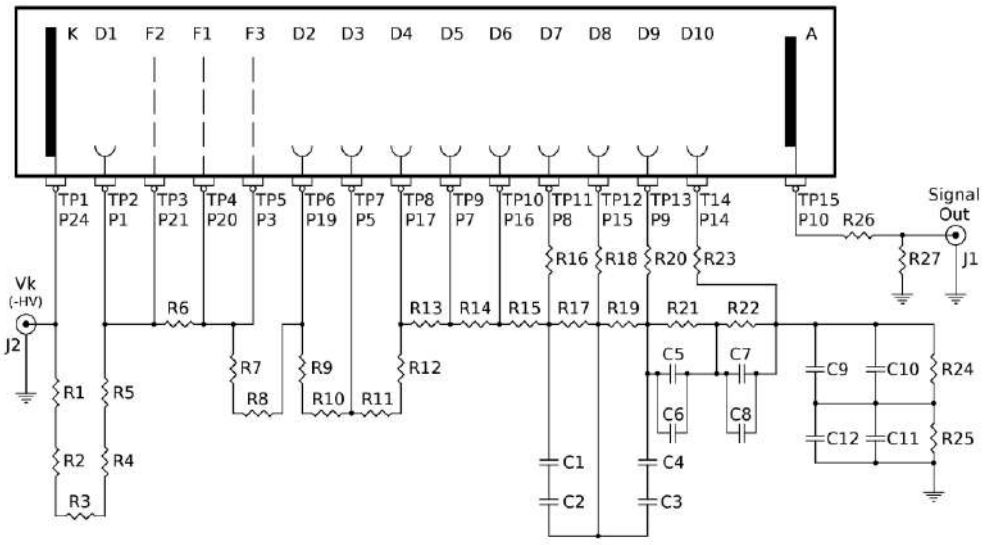

Figure 5.3: *PMT Voltage Divider [44]*

5.2.3 Reference Light Measurement

The RkP-465 probe connected to the Rm-3700 bolometer was used to measure the intensity of light and verify the stability of the laser. We used this absolute luminosity measurement as a relative reference measurement, to monitor and correct whatever light fluctuation affected the PMT signal from instabilities of the laser diode source. Any light fluctuations

Electrodes	Ratio
K-D1	16.8
D1-F2	0
F2-F1	0.6
F1-F3	0
F3-D2	3.4
D2-D3	5
D3-D4	3.33
D4-D5	1.67
D5-D6	1
D6-D7	1.2
D7-D8	1.5
D8-D9	2.2
D9-D10	3
D10-A	2.4

Table 5.1: *Voltage distribution ratio [41, 44]*

affected the PMT signal, but normalization was applied to account for these variations. The bolometer was also connected to the DAQ Monitor via an RS-232 serial cable, and data was acquired through the LabVIEW interface (see Section 5.3).

5.2.4 Preliminary Test

Initially, we conducted preliminary tests. First, each measuring instrument was tested separately. Then, the setup was assembled in a dark room without any temperature control.

The PMT was held in place by a custom-made support. This support holds the PMT on one side, while on the other side, there is a support for the optical fiber. The support allows the distance between the PMT and the fiber to be adjusted (Fig. 5.4 (left)).

Attached to the fiber, there is a custom-made container that holds the optical filters. Finally, a diffuser is placed at the fiber output.

During the preliminary tests, we first determined the optimal distance

at which to place the diffuser to ensure uniform illumination across the entire photocathode surface. Then, we tested various filter configurations to achieve the desired initial anodic current ($\sim 28\ \mu A$).

During testing, we noticed that despite being in a dark room, some background light pulses were present with the laser off. This led us to design a light-blocking cone, shown in Fig. 5.4 (right), and later, an entire light-blocking box.

Figure 5.4: *Some photos taken during the testing phase in the dark room.*

After completing all the tests, we installed the experimental set-up in the climatic chamber.

5.3 Implementation of the Data Acquisition System

I designed and developed the data acquisition system, whose LabVIEW front panel is shown in Fig. 5.5, that allows synchronized measurements both of the anode current by the Keithley multimeter and the reference light intensity by the bolometer.

Data sampling was set to 0.2 s, ensuring synchronization within 0.2 s margins due to logical processing times. Given that the measured quantities vary on long timescales, minor timing misalignments were negligible. Data were averaged over at least on one minute for the analysis.

Figure 5.5: *LabVIEW DAQ Front Panel*

The system stored data in ".txt" format, saving a file every 5 minutes for security purposes. The LabVIEW timestamp was used for time logging. Furthermore, remote access to the acquisition system allowed for real-time monitoring and control.

Later, an Arduino-Uno was employed for the automatic temperature reading via a Type-K thermocouple data acquisition. This function was not integrated into the main system but was synchronized offline during the analysis. the The climatic chamber can also record the temperature

values over time but that the values are slightly different from those measured with the thermocouple because the latter one was in proximity of the photocathode surface.

5.4 Measurements and Results

To perform a stress test, the PMT HV (the gain) and the photon flux were adjusted to give a high anodic current ($\sim$ 28 μA). The single measurement plan required a long-lasting data acquisition (50-70 hours), to allow the collection of 5-7 C of anodic charge and emulate the operational conditions of FNAL, observed in Fig. 4.2. Stability tests over time were performed at room temperature and at low temperatures with laser ON. Moreover, dark-current measurements were taken under identical conditions but laser OFF. The measurement results will be discussed below.

5.4.1 Light Stability

Looking at the light intensity measurements performed with the bolometer, they confirmed the high stability of the laser source. The plot in Fig. 5.6 is a typical example of how laser light remains stable also during cooling cycles. Nevertheless, we used the bolometer measurement to normalize the synchronized PMT anodic current data and correct the very small fluctuations in the laser source intensity.

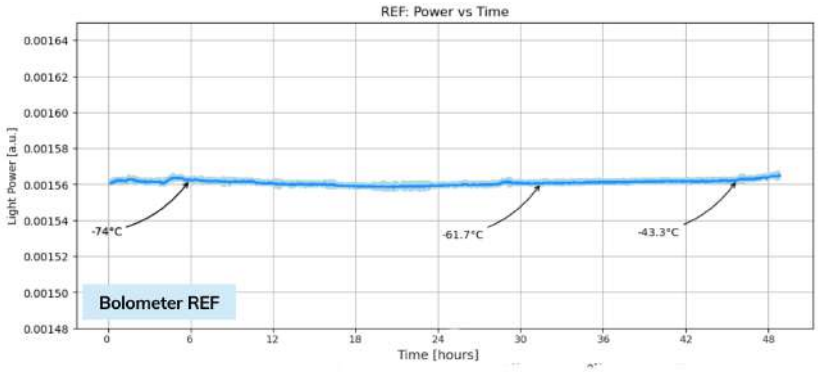

Figure 5.6: *Example of laser light stability during a cooling cycle.*

5.4.2 Gain Stability at Room Temperature

Our measurements confirm the stability of the PMT gain at room temperature, as also observed in the PMT system installed at FNAL. The top plot in Fig. 5.7 shows the typical behavior of the anodic current under dark conditions, while the bottom plot displays the normalized current with the ON laser beam [32]. The dark current measurements at cryogenic temperature show stability, albeit at lower current values.

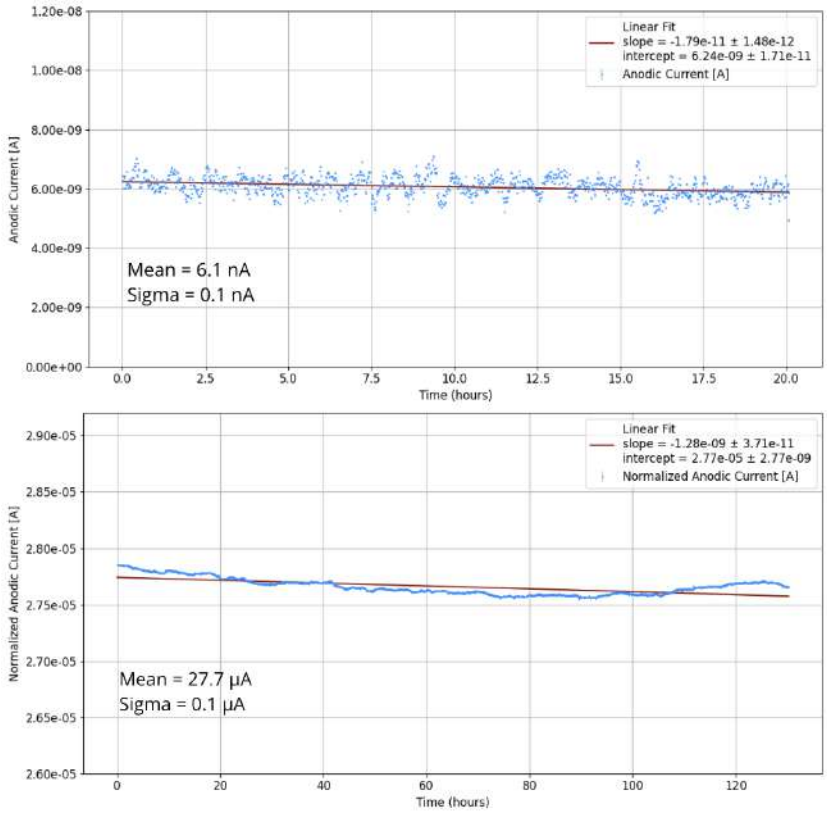

Figure 5.7: *Top: Dark anodic current at room temperature over 20 hours. Bottom: Normalized anodic current (with respect to the light reference) over 5.5 days (room temperature) [32].*

5.4.3 Gain Loss at Low Temperature

We performed two sets of measurements, one in 2023 and another in 2024, under different gain and illumination conditions. In the 2024 measurements, the PMT was exposed to a higher light intensity and operated at a lower voltage than in 2023. The different conditions and the results obtained are summarized in Table 5.2.

During each cooling cycle, we identified three distinct phases of the normalized anodic current behavior over time. The plot shown in Fig.

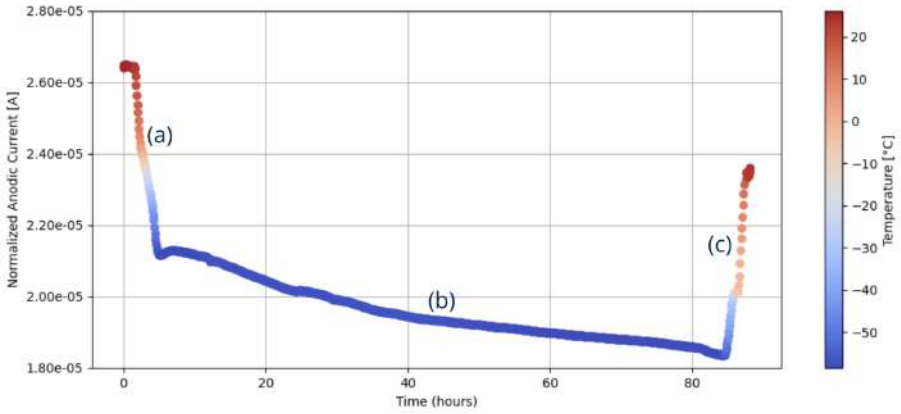

Figure 5.8: *Normalized anodic current (with respect to the light reference) at different temperatures. (a) From room temperature to -60° C in 3 hours. (b) At -60° C for 80 hours. (c) From -60° C back to room temperature in 3 hours [32].*

5.8) corresponds to the fourth cooling cycle as a representative example of the three phases [32]:

(a) Gain loss during cooling from room temperature;

(b) Gain loss at a fixed low temperature (Table 5.2);

(c) Gain recovery during temperature increase.

The gain in phase (a) decreases with a slope of $\sim 6 \times 10^{-8}$ A/° C. This loss is recovered in phase (c) as the temperature increases, following the same slope. However, during phase (b), an irreversible loss is observed: no gain recovery occurs when the PMT room temperature is restored.

Long-term low-temperature thermostatic measurements clearly show the effects of PMT fatigue/aging [32].

The fact that PMTs lose gain at cryogenic temperatures is well known in the literature [55, 56]. In general, this loss is reversible. It can be attributed to temperature-dependent factors that affect PMT performance. These include variations in quantum efficiency, changes in electron mobility that impact dynode multiplication, and reduced thermionic emission, which lowers both noise and signal. Furthermore, cooling reduces the dark current as a result of the decrease in thermal carrier generation.

Some Comments on Cooling Cycles

- **1st Cooling:** The cooling phase lasted less than 24 hours due to instabilities in the chamber, which caused the temperature to rise. These instabilities were resolved by thermally insulating the chamber connectors.
- **2nd Cooling:** First long-duration measurement. After 95 hours, we increased the supply voltage to restore the initial current level.
- **3rd Cooling:** The thermocouple temperature measurement was introduced.
- **4th, 5th, and 6th Cooling:** The PMT had already undergone some degradation, as the chamber exhibited slight instability over long periods in the first set of measurements at low temperature. The voltage was set lower, and the illumination was set higher than before. The configuration was chosen to restore the initial anodic current level.

In Table 5.2, a summary of the results of the two sets of measurements is shown. Interestingly, in both sets of measurements (2023 and 2024), the gain loss per anodic charge decreases over time. This indicates that as the PMT undergoes repeated cooling cycles, the degradation effect becomes less pronounced. In the 2023 dataset, the first cooling results in a loss/charge of 3.86%, while subsequent cycles show a gradual reduction in the percentage loss per collected charge. The same trend is observed in

		Temperature (°C)	Duration (h)	HV (V)	Gain loss (%)	Anodic Charge (C)	Gain loss / charge (%/C)
2023	1st Cooling	-74	20	1575	7.29 %	1.89	3.86 %
	2nd Cooling part 1	-70	95	1575	12.50 %	6.81	1.84 %
	2nd Cooling part 2	-70	20	1675	3.05 %	2.11	1.45 %
	3rd Cooling	-66	150	1675	16.60%	16.60	1.00 %
2024	4th Cooling	-60	45	1520	19.68%	3,49	5.41%
	5th Cooling	-60	80	1520	13.39 %	4.20	3.18%
	6th Cooling	-60	63	1520	8.88 %	3.87	2.29 %

Table 5.2: *Summary of data sets and results [32].*

the 2024 dataset, where the percentage of gain loss per charge decreases from 5.41% in the fourth cooling to 2.29% in the sixth cooling.

5.4.4 Reproducibility

It is interesting to compare the data from the 2nd and 5th cooling cycles as they are shown in Fig. 5.9.

These measurements were performed under different light and voltage conditions, but they all share the same initial anode current. For comparison, we limit the analysis to the first 80 hours of the first measurement and compare it with the second one. The trend, as shown in the plot in Fig. 5.10, clearly indicates a high degree of correlation between the two datasets, despite the different operational conditions. This suggests that the observed behavior is primarily driven by the anode current rather than by individual dependence from light intensity or applied voltage.

In the second measurement, the PMT was more degraded because it had already undergone several stress measurement cycles, which had led to a decrease in its gain. The higher light intensity allowed us to reach the same anode current, with the voltage appropriately adjusted. However, in this case, there is more light and so more p.e. emitted by the photocathode but less multiplication. Therefore, eventually the current on the last dynodes and the anode current are approximately the same.

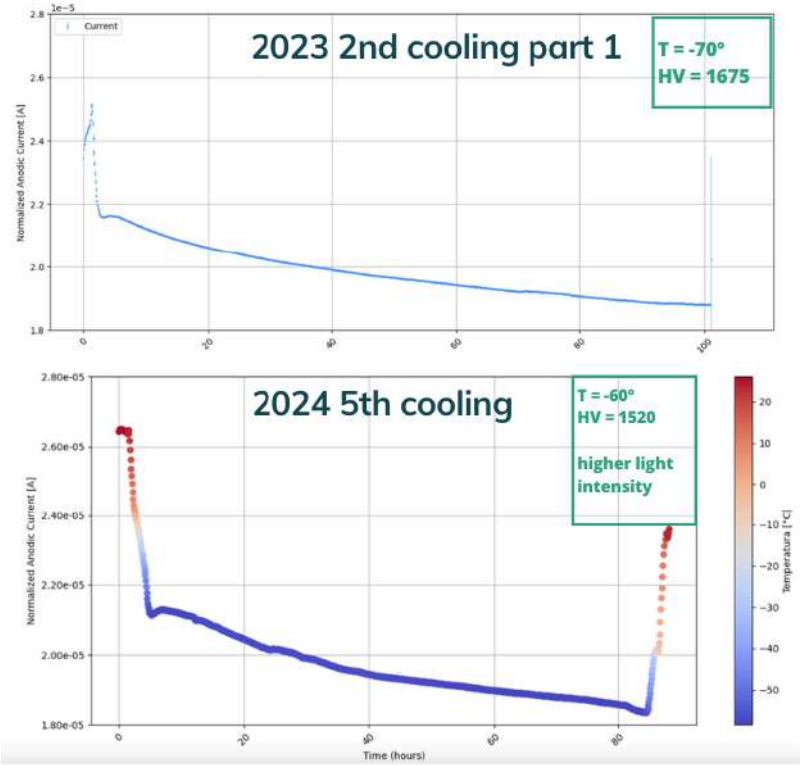

Figure 5.9: *Normalized Anodic Current of 2nd and 5th cooling cycle*

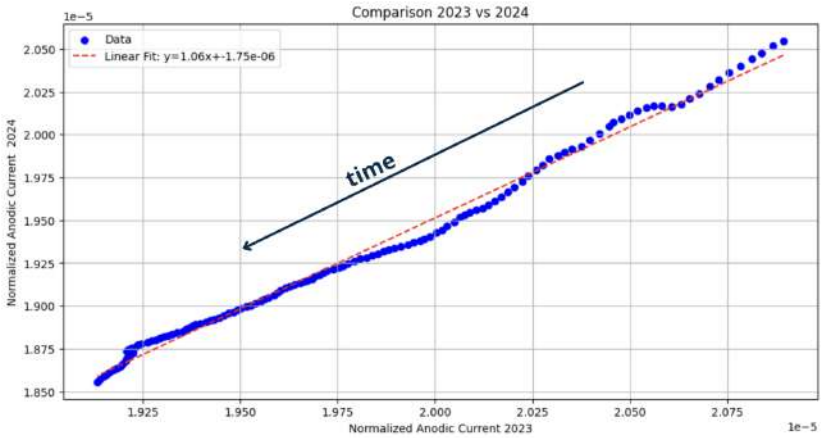

Figure 5.10: *Time correlation of the 2nd and 5th datasets*

5.5 A Simple Model

A naive model is under investigation to describe the observed gains loss trends, considering the irreversible components of degradation. We consider the equation 3.4 where, in the most general case, A and α are different for each dynode:

$$G = \prod_{i=1}^{n} A_i V_i^{\alpha_i} = \prod_{i=1}^{n} A_i (\epsilon_i V)^{\alpha_i} \tag{5.1}$$

The idea is that all dynodes have the same initial conditions but over time they can suffer a degradation in the secondary emission coefficient. From various experimental hints, we can reasonably hypothesize that the degradation of the dynodes depends on the amount of current at their stage. However, only the last dynodes in the chain should impact on the total gain loss, since the first dynodes receive much less current and therefore degrade less. This degradation alters the parameters of the secondary emission coefficient, specifically A or α.

In Model A, we assume the coefficient A to decrease proportionally to the current in each multiplication stage. This loss factor acts every time an electron strikes a dynode and is applied individually for each dynode over various time steps. A similar loss factor was also introduced for the coefficient α in Model B. The simulation uses the known voltage divider data to model the dynode multiplication chain [41].

The initial gain was derived from the gain-voltage characterization curve (see Section 5.2.1) and set to:

$$G = 1.11 \cdot 10^7$$

at the voltage of 1575 V used during the first cooling cycle.

As shown in Fig. 5.11 (bottom), Model A - i.e. a loss factor proportional to the current affecting the parameter A - better reproduces the observed degradation trend. This seems reasonable because α depends on the material of the dynodes, which we do not expect to change significantly at low temperatures. Instead, in multilayer dynodes, mismatches in the thermal expansion coefficients of different materials can induce significant mechanical stress at low temperatures, potentially leading to

microcracks or delamination when several accelerated electrons impinge on them. This surface degradation can be expressed as a decrease in the factor A [57].

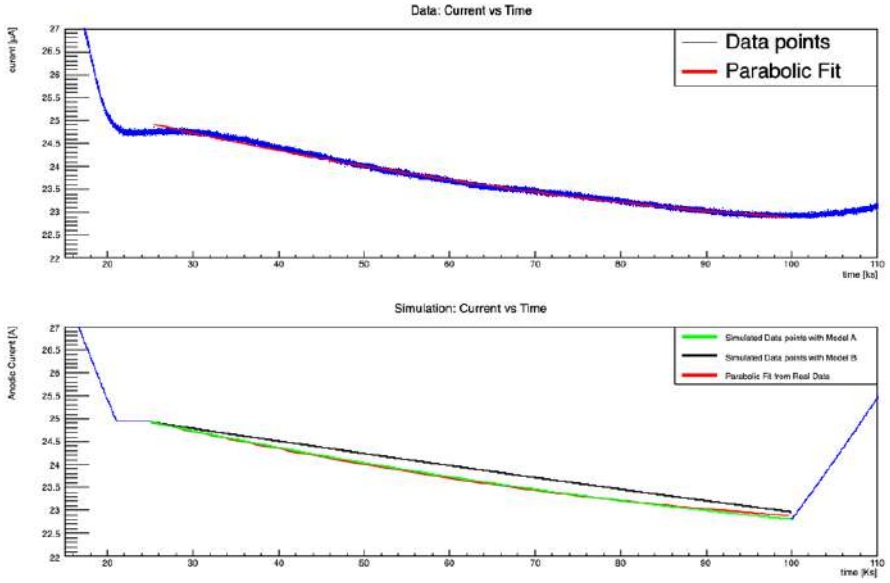

Figure 5.11: *Top: Experimental data from the first cooling phase, fitted with a parabolic fit with equation* $y = (26.0919 \pm 0.002) - (0.0513182 \pm 0.00007)\, x + (0.00019218 \pm 0.0000005)\, x^2$. *Bottom: Comparison between two degradation models. The fit from the top graph is included for reference. The reduced chi-squared between the fit and Model A is* $\chi^2/\mathrm{ndf} = 0.07$.

Chapter 6

Conclusions

The objective of my thesis work was to analyze the performance of the Hamamatsu R5912-MOD photomultiplier tubes used in the ICARUS Light Detection System, focusing on the observed gain loss as an aging effect under liquid argon cryogenic conditions at 87 K. Observations at FNAL indicate that the gain loss is influenced by both the signal intensity and the gain:

- A reduction in loss was observed after the construction of the 2.85 m thick concrete overburden.
- Lowering the high voltage (HV), and thus the gain, also reduced the gain loss.
- Despite the reduction in gain, the PMTs remained equalized.

The mitigation strategies implemented within the ICARUS detector to address and mitigate this effect — the lowering of PMT high voltage, the improvements in PMT response due to a new cabling system, and the construction of the overburden — have led to a consistent limitation in thegain loss, reducing the values from the initial 1.93% per month to the current 0.31% per month.

Using an environmental high volume chamber at the INFN Catania Section, I developed a suitable experimental setup for PMT testing at low temperature. Our experimental study shows a gain loss similar to that

observed by ICARUS at FNAL, at temperatures around $-60/-70\,^{\circ}$C, which, although higher than the liquid argon temperature, still confirms a clear temperature dependence. No gain loss was observed at room temperature, but at lower temperatures the observed gain loss is permanent and depends on factors such as the amount of anodic current in the PMT. Specifically, we note that:

- The loss, observed even at higher temperatures than at FNAL, is a permanent loss.
- The loss depends on the light signal (no losses are observed in the dark current, even at cryogenic temperatures).
- No loss is seen at room temperature.
- For subsequent measurements under the same conditions, the loss decreases.

Based on Hamamatsu guidelines and our simulations, degradation of the last dynodes at low temperature appears to be a plausible cause of the gain loss. However, further investigations are necessary under varied experimental conditions to fully explain the irreversible nature of the gain loss. It would be interesting, for example, to discern any contributions deriving from the variation of the quantum efficiency (QE), because the measurements carried out in Catania are related to the anodic current, where the contribution of the QE is indistinguishable.

A critical aspect of this work was related to some instabilities of the climatic chamber at low temperature over time. Technical interventions were frequently requested to restore normal operating conditions. A more systematic study of the PMT gain loss under different thermal conditions and different voltages would be desirable.

This research also paid special attention to the implications for the long-term durability of the PMTs both for the ICARUS experiment and for future applications. For instance, the SBND detector uses R5912-MOD PMTs (with X-ARAPUCA dichroic filters), and ProtoDUNE employs Hamamatsu R5912-02 PMTs with 14 dynodes. The insights gained from our study are therefore valuable not only for ICARUS but also for other upcoming experiments.

In summary, our findings demonstrate that the implemented mitigation strategies significantly reduce the gain loss, and the testing system developed will serve as an indispensable tool for future studies involving photomultipliers in cryogenic conditions.

Acknowledgments

I would like to thank all those who contributed to this thesis and to the achievement of my degree — finally!

First of all, I would like to thank the INFN Catania group. In particular, I am deeply grateful to my supervisor, Prof. Catia Petta, for her guidance, support, and for all the understanding and humanity she consistently shows toward students, both from a professional and a personal perspective.

I warmly thank F. Librizzi, A. Grimaldi, and D. Sciliberto for the significant technical support provided during the measurements and for assisting me throughout the thesis work, as well as Dr. V. Brio and Dr. R. Persiani for their help during data taking and analysis.

I would also like to thank the INFN Pavia group, who helped in setting up the work reported in this thesis. I am especially grateful to Dr. G.L. Raselli, my co-supervisor, for his scientific support and exceptional availability, and to Dr. M. Rossella for his valuable collaboration.

I sincerely thank Dr. D. Torretta for warmly welcoming me and supporting me during my stay at Fermilab.

I would also like to thank Dr. A. Di Mattia for the climatic chamber, which was crucial for the experimental work conducted in this thesis.

Finally, I would like to thank Dr. M. Vicenzi and Dr. A. Scarpelli for their analysis of the PMT data at FNAL, which I report and discuss in this thesis.

Bibliography

[1] W. Pauli, *Dear radioactive ladies and gentlemen*, (1930).

[2] B. Povh et al., *Particles and Nuclei* (Springer-Verlag, Berlin Heidelberg, 2015), pp. 167–184.

[3] Basudeb Dasgupta and Joachim Kopp, *Sterile neutrinos*, Physics Reports **928**, 1 (2021), sterile neutrinos.

[4] Sakata Maki, Nakagawa, *Remarks on the Unified Model of Elementary Particles* (Progress of Theoretical Physics, Oxford, 1962), Vol. 28.

[5] Pedro A.N. Machado, Ornella Palamara, and David W. Schmitz, *The Short-Baseline Neutrino Program at Fermilab*, Annual Review of Nuclear and Particle Science **69**, 363 (2019).

[6] H. Minakata and S. J. Parke, *Neutrino Oscillations and CP Violation*, Physical Review D **83**, 093008 (2011).

[7] L. Wolfenstein, *Neutrino Oscillations in Matter*, Physical Review D **17**, 2369 (1978).

[8] S. P. Mikheyev and A. Yu. Smirnov, *Resonance Amplification of Oscillations in Matter and Spectroscopy of Solar Neutrinos*, Soviet Journal of Nuclear Physics **42**, 913 (1985), english translation in: Nuovo Cimento C, 9 (1986) 17.

[9] Y. Fukuda et al., *Evidence for Oscillation of Atmospheric Neutrinos*, Physical Review Letters **81**, 1562 (1998).

[10] Q. R. Ahmad et al., *Measurement of the Rate of $\nu_e + d \rightarrow p + p + e^-$ Interactions Produced by ^8B Solar Neutrinos at the Sudbury Neutrino Observatory*, Physical Review Letters **87**, 071301 (2001).

[11] A. Osipowicz et al., *KATRIN: A Next Generation Tritium Beta Decay Experiment with Sub-eV Sensitivity for the Electron Neutrino Mass*, Nucl. Instrum. Meth. A **523**, 275 (2004).

[12] Carlo Giunti, *Fundamentals of Neutrino Physics and Astrophysics* (Oxford University Press, New York, 2007).

[13] R. Wendell, *Atmospheric Results from Super-Kamiokande* (IP Conf., Proc., 2015), No. 1.

[14] G. Giacomelli, *Neutrino physics and astrophysics with the MACRO experiment at the Gran Sasso lab* (Braz., J. Phys., 2003), Vol. 33.

[15] I. Esteban et al., *The fate of hints: updated global analysis of three-flavor neutrino oscillations*, Journal of High Energy Physics **2020**, 178 (2020).

[16] NOvA Collaboration, *Latest results on neutrino oscillations from NOvA*, Proceedings of the Neutrino 2020 Conference (2021).

[17] T2K Collaboration, *Constraint on the matter–antimatter symmetry-violating phase in neutrino oscillations*, Nature **580**, 339 (2020).

[18] DUNE Collaboration, *Long-Baseline Neutrino Facility (LBNF) and Deep Underground Neutrino Experiment (DUNE)*, arXiv preprint (2016).

[19] JUNO Collaboration, *JUNO Conceptual Design Report*, arXiv preprint (2016).

[20] KATRIN Collaboration, *Direct neutrino-mass measurement with sub-electronvolt sensitivity*, Nature Physics **18**, 160 (2019).

[21] Planck Collaboration, *Planck 2018 results: Cosmological parameters*, Astronomy & Astrophysics **641**, A6 (2020).

[22] R. Acciarri et al., *A Proposal for a Three Detector Short-Baseline Neutrino Oscillation Program in the Fermilab Booster Neutrino Beam*, (2015).

[23] A. P. Serebrov, R. M. Samoilov, and M. E. Chaikovskii, Analysis of the result of the Neutrino-4 experiment in conjunction with other experiments on the search for sterile neutrinos within the framework of the 3 + 1 neutrino model, 2022.

[24] Francesco Poppi, *Status and perspective of ICARUS-T600 detector at the Fermilab Short-Baseline Neutrino program*, Nucl. Instrum. Meth. A **1072**, 170113 (2025).

[25] Carlo Rubbia, *The Liquid Argon Time Projection Chamber: A New Concept for Neutrino Detectors*, CERN-EP-INT-77-08 (1977).

[26] F. Tortorici; V. Bellini; C. Petta; C. M. Sutera, *The ICARUS Experiment*, Elsevier (2018).

[27] Cern Neutrino to Gran Sasso, `http://proj-cngs.web.cern.ch/proj-cngs/ProjetOverview/projetoverview2002.htm` .

[28] Inaugurazione, `http://icarus.lngs.infn.it/inauguration.php` .

[29] Biswaranjan Behera, *The Search for Short Baseline Neutrino Oscillation with the ICARUS Detector*, Physical Sciences Forum **8**, (2023).

[30] ICARUS, *ICARUS Detector Overview*, `http://icarus.lngs.infn.it/DetectorOverview.php` .

[31] B. Ali-Mohammadzadeh et al, *Design and implementation of the new scintillation light detection system of ICARUS T600*, JINST **15**, T10007 (2020).

[32] C. Saia, V. Brio, R. Persiani, C. M. A. Petta, G. L. Raselli, M. Rossella, and M. Vicenzi, *Gain stability of Hamamatsu R5912-MOD photomultipliers at low temperature*, Nucl. Instrum. Meth. A **1069**, 169861 (2024).

[33] A. Aduszkiewicz et al., *Design and Implementation of the Cosmic Ray Tagger System for the ICARUS detector at FNAL*, (2025).

[34] Ettore Segreto, *Properties of liquid argon scintillation light emission*, Phys. Rev. D **103**, 043001 (2021).

[35] P et al. Benetti, *Measurement of the specific activity of 39Ar in natural argon*, Nucl. Instrum. Meth. A **574**, 83–88 (2007).

[36] C. Rubbia, Searching for short baseline anomalies with the LAr-TPC detector at shallow depths, 2014.

[37] L. et al. Bagby, *Overhaul and installation of the ICARUS-T600 liquid argon TPC electronics for the FNAL Short Baseline Neutrino program*, Journal of Instrumentation **16**, P01037 (2021).

[38] W. Badgett et al., *The electronic set-up for the scintillation light detection system of ICARUS-SBN at Fermilab*, Nucl. Instrum. Meth. A **1047**, 167871 (2023).

[39] *V1730 / V1730S Datasheet*, CAEN .

[40] G.L. Raselli et al., *Time calibration and synchronization of the scintillation light detection system in ICARUS-T600*, Journal of Instrumentation **19**, C01027 (2024).

[41] *PMT R5912 Datasheet*, Hamamatsu Photonics K.K. (2011).

[42] M. Babicz et al., *Timing properties of Hamamatsu R5912-MOD photomultiplier tube for the ICARUS T600 light detection system*, Nucl. Instrum. Meth. A **912**, 231 (2018), new Developments In Photodetection 2017.

[43] M. Babicz et al., *Linearity and saturation properties of Hamamatsu R5912-MOD photomultiplier tube for the ICARUS T600 light detection system*, Nucl. Instrum. Meth. A **936**, 554 (2019), frontier Detectors for Frontier Physics: 14th Pisa Meeting on Advanced Detectors.

[44] M. Babicz et al., *Test and characterization of 400 Hamamatsu R5912-MOD photomultiplier tubes for the ICARUS T600 detector*, JINST **13**, P10030 (2018).

[45] *Photomultipliers Tubes Basics and Applications*, Hamamatsu **4-th edition**, (2017).

[46] J. Budagov F. Cervelli I. Chirikov-Zorin M. Incagli D. Lucchesi C. Pagliarone S. Tokar F. Zetti E.H. Bellamy, G. Bellettini, *Absolute calibration and monitoring of a spectrometric channel using a photomultiplier*, Nucl. Instrum. Meth. A **339**, 468 (1994).

[47] *N126 High Voltage Power Supply Technical Information Manual*, CAEN .

[48] *CPS520 Laser Datasheet*, Thorlabs (2014).

[49] *PE1535 Bench Model Power Supply Operating Manual*, Philips (1982).

[50] *Keithley 6517B Reference Manual*, Keithley (2016).

[51] *Rm-3700 Universal Radiometer Operating Instruction*, Laser Probe Inc. (1992).

[52] *RkP-465 Silicon Power Probe Datasheet*, Laser Probe Inc. (1992).

[53] *MAX31856 Precision Thermocouple to Digital Converter Datasheet*, Analog Devices Inc./Maxim Integrated (2015).

[54] *CK-120 Opitcal Fiber Datasheet*, Mitsubishi Chemical Corp. (2019).

[55] M. Prata, M.C. Prata, G.L. Raselli, M. Rossella, and C. Vignoli, *Performance and behaviour of photomultiplier tubes at cryogenic temperature*, Nucl. Instrum. Meth. A **567**, 222 (2006), proceedings of the 4th International Conference on New Developments in Photodetection.

[56] A. Ankowski et al., *Characterization of ETL 9357FLA photomultiplier tubes for cryogenic temperature applications*, Nucl. Instrum. Meth. A **556**, 146 (2006).

[57] B.F. SØrensen, S. Sarraute, O. JØrgensen, and A. Horsewell, *Thermally induced delamination of multilayers*, Acta Materialia **46**, 2603 (1998).